이학석사학위논문

Photo-switchable Molecular Device Activated by Perovskite/Graphene Heterostructure

페로브스카이트/그래핀 이종 접합구조를 활용한 광반응성 분자 소자

2023년 2월

서울대학교 대학원

물리천문학부

이 창 준

Photo-switchable Molecular Device Activated by Perovskite/Graphene Heterostructure

페로브스카이트/그래핀 이종 접합구조를 활용한 광반응성 분자 소자

지도교수 이 탁 희

이 논문을 이학석사석사 학위논문으로 제출함

2023 년 2 월

서울대학교 대학원

물리천문학부

이 창 준

이창준의 이학석사석사 학위논문을 인준함

2023 년 2 월

위 원 장 _____ 홍 승 훈 _____ (인)

부위원장 _____ 이 탁 희 _____ (인)

위 원 _____ 최 현 용 _____ (인)

Photo-switchable Molecular Device Activated by Perovskite/Graphene Heterostructure

by

Changjun Lee

A Dissertation Submitted to the Faculty of the Graduate School of Seoul National University in Partial Fulfillment of the Requirements for the Degree of Masters of Science

Feburary 2030

Advisory Committee:

Professor Seunghun Hong, Chair
Professor Takhee Lee, Advisor
Professor Hyunyong Choi

The manuscript printed and bound in the present form is intended for personal use and distribution among the author's colleagues, friends, and family.

An electronic copy of the document has been submitted to the Seoul National University Library with minor formatting adjustments in compliance with the University's requirements.

This dissertation contains contents of the following journal publications:
C.Lee et al., *Adv. Opt. Mat.* 2022, 10, 2200049.;
List valid at the time of submission—Material from the dissertation may produce one or more additional publications in the future.

A catalogue record is available from the National Library of Korea

Printed in Republic of Korea

Abstract

Photoresponsivity is a fundamental process that constitutes optoelectronic devices. In molecular electronic devices, one of the most adopted strategies is to employ photoactive molecules that can undergo conformational change upon light illumination as the conduction channel. However, such devices suffer from their relatively low photoresponsivity, long switching time, and unidirectional switching. In this thesis, I employed organohalide perovskite (OHP)/graphene heterojunction as a photoactive electrode that acted a source of photo-generated carriers collected as photocurrent in self-assembled monolayer (SAM)-based molecular junctions. This hybrid device architecture of perovskite/graphene/SAM allows the molecular junctions to attain a high photoresponsivity with molecules that have intrinsically little photo-response. I elucidate the role of the molecular SAM in enhancing the photoresponsivity by systematically examining the charge transfer processes at the graphene/SAM interface via molecules with different intrinsic dipole moments. Corroborated with a theoretical analysis, this revealed the origin of the observed photoresponsivity as light-induced coupling between the SAM and the OHP/graphene electrode within the orbital-mediated resonant tunnelling transport regime. These findings advance our understanding of photo-induced charge transport in molecular junctions with heterointerfaces, providing a road-map for designing high-performance molecular optoelectronic devices based on hybrid device architecture.

Keywords: Molecular Electronics, Photo-switching, Organic Halide Perovskite, Self-assembled Monolayer, Graphene Electrode, Resonant Tunnelling

Student ID: 2020-21713

Contents

List of Figures

calculated XRD data (COD ID 2107954).[76]Powder XRD spectra of simulated and synthesized $MAPbI_3$ powder.

Figure 4. shows the characterization of deposited $MAPbI_3$ film. The surface roughness was turned out to be ~3.3 nm. The absorption edge was estimated at ~772 nm (optical bandgap ~1.6 eV), which means that $MAPbI_3$/graphene absorbs the full visible range (400–700 nm).[77] (a) AFM image of deposited MAPbI3 film. (b) Absorbance spectra of deposited $MAPbI_3$ film.

Figure 5. (a) UPS spectra of the $MAPbI_3$ film using the single-source flash evaporation method and the monolayer graphene. (b) Energy band diagram when the graphene and $MAPbI_3$ form a contact. (c) PL spectra of the pristine $MAPbI_3$ film and $MAPbI_3$/graphene heterostructure upon 532 nm excitation. (d) I_{ds}–V_{gs} characteristics of a pristine GFET (denoted as Gr, black curve) and $MAPbI_3$/graphene hybrid FET (denoted as $MAPbI_3$/Gr, red curve). The inset shows the schematic image of a $MAPbI_3$/Gr FET device. (e) I_{ds}–V_{gs} curves of a $MAPbI_3$/Gr FET showing a gradual p-doping effect as the light intensity increases. (f) Electrical characteristics of a control device ($MAPbI_3$/graphene/Au without SAM) under the light intensity of 3.82 mW/cm^2. The left inset shows the I–V curve on linear scale and the right inset presents the schematic image of the fabricated control device

Figure 6. (a) The logarithmic average current densities according to the voltage for PFBT. Blue and orange lines represent the dark current and photocurrent, respectively. (b) Statistical data and its Gaussian fitting of logarithmic current densities of all Au/PFBT/Graphene molecular junctions under the dark(black) and light-illuminated (red) conditions. They were measured before MaPbI3 being deposited above

Figure 7. (a) I–V characteristics of the representative BPT-based molecular junction according to the light intensity. (b) Photocurrent (= current when illuminated – current at dark condition) and photo responsivity data plot of Au/BPT/Graphene/$MAPbI_3$ junction. (c, d) Statistical data with Gaussian fitting of logarithmic current densities of all BPT molecular junctions under the (c) dark and (d) light conditions. The mean logarithmic current densities at 1 V were represented as green dashed lines.

Figure 8. Statistical data of (a, c) BDT and (b, d) PFBT-based molecular junctions at 1 V.

Figure S11 represents statistical data of all molecular junctions at the bias of -1V. Under the dark condition, average logarithmic current densities (Log J) were 3.21 for BPT, 3.19 for BDT, and 3.73 for PFBT, respectively. With the light illumination, the Log J values were 3.3 for BTP, 3.3 for BDT, and 4.44 for PFBT, corresponding to ~123 % current enhancement for BDT, ~128 % for BDT, and ~513 % for PFBT.

Figure 9. Statistical data of (a, b) BPT, (c, d) BDT, and (e, f) PFBT-based molecular junctions at -1V.

Figure 10. Switching characteristics of (a) BPT (measured at 0.8 V), (b) BDT (at 0.8 V), and (c) PFBT (at 0.5 V) molecular junctions under light intensity of 0.64 mW/cm^2. (d) Multiple switching characteristics of a PFBT junction measured at 0.25 V under light intensity of 64 $\mu W/cm^2$.

Figure 11. Photo-induced current enhancement by dipole-induced field variation. (a, b) Schematic mechanism of photo-induced current enhancement by variating dipole moments. Band diagrams of (a) BPT-based and (b) PFBT-based molecular junction. (c, d) Logarithmic

average current densities according to the voltage for (c) BDT and (d) PFBT molecular junctions. Red and black lines represent the photocurrent and dark current, respectively. (e) PL quenching characteristics according to the dipole direction. (f) TRPL spectra of perovskite/graphene/SAM structure according to the dipole moment variation.

Figure 12. (a) UPS data of SAM-treated Au films. (b) Schematic band diagram for SAM-treated Au films.

Figure 13. KPFM data of (a) BPT-treated, (b) BDT-treated, (c) pristine, (d) PFBT-treated Au films. (e) Pixel analysis for all SAM-modified Au films.

Figure 14. *I–V characteristics of a C8-based molecular junction.*

Figure 15. (a, b) Fitting results of average I–V curves for (a) BPT and (b) PFBT molecular junctions by using Landauer formula. Black open circles: fitted I–V curves of the dark condition. Red open triangles: experimental data of the dark condition. Blue filled circles: fitted I–V data of the light condition. Green filled triangles: experimental curves of the light condition. (c, d) Schematic illustration of the charge transport modulation mechanism for (c) BTP and (d) PFBT molecular junctions.

Figure 16. I–V curve fitting of BDT-based molecular junctions.

Figure 17. From the Au/PFBT/graphene heterostructured sample, I extracted (a) peaks of C-F bonds in C1s XPS. (b) peaks of C-F bonds in F1s XPS.

List of Table

1. Introduction

In the field of molecular electronics, various studies have been conducted to achieve the ultimate miniaturization of electronic circuits.[1-8] Many significant developments have been made to utilize single or bundles of molecules as electronic components such as molecular wires, rectifiers, transistors, memories, switches, and thermoelectric devices.[9-18] Regardless of the types of devices, it is crucial to understand and control the charge transport characteristics through molecular junctions. Charge transport phenomena in molecular junctions are influenced by not only the electrical characteristics of molecules but also the interactions that occur at the interfaces between molecules and electrodes.[19-23] Therefore, taking into account the electrical properties of the electrodes and their interaction with molecules, the choice of electrode material is important in determining the overall charge transport properties of the molecular junctions.

Since the self-assembled monolayers (SAMs) of molecules are typically chemisorbed onto the bottom electrodes, the choices of the bottom electrodes are limited; for example, the end groups of molecules such as thiol group form covalent bonding on the electrodes such as Au and Ag.[24] For this reason, changing top electrodes has been used as a preferred way to tailor the charge transfer through molecular junctions. Several materials and methods have been suggested as top electrodes of molecular junctions, such as liquid metals, evaporated or transferred metals, conducting polymers, graphene film, etc.[25-27] The development of these junctions has contributed to producing stable molecular junctions with high yield and enabled charge transport modulation using engineering treatments for the top electrodes.[28,29] However, once a molecular junction is manufactured, these conductive materials of electrodes have a

fixed work function regardless of using pristine or engineered materials, thus limiting the further modulation of charge transport properties of the molecular junctions.

In this context, illuminating light can be an attractive tool to make in-situ controllable molecular junctions due to its continuous characteristics, good addressability, and compatibility with solid-state device structures. Conventionally, optical control of the charge transport in a molecular junction was implemented by employing intrinsically photo-active molecules whose molecular conformation changes upon photo-excitation.[30-32] However, SAM-based molecular junctions with photo-switching molecules suffer from either long switching times or irreversible switching properties.[33-35] Therefore, rather than relying on the intrinsically photo-active molecules, functionalizing other device components (e.g., electrodes) can be a suitable engineering option to explore the photo-modulated conduction properties in molecular junctions.

In order to effectively achieve photo-modulated charge transport characteristics of molecular junctions via engineering the electrodes, a well-designed electrode with the following features are required: high light absorption coefficient, efficient carrier photo-generation, and effective charge transfer to the active SAM. In this regard, organo-halide perovskite (OHP) is an excellent candidate as a photo-active layer that can be integrated to the top electrode of the molecular junctions. OHPs have recently attracted significant attention due to their outstanding photophysical properties, such as their high absorption coefficient, low exciton binding energy, and long carrier lifetime.[36-38] Owing to their high quantum efficiency, numerous carriers can be generated when exposed to light, which can enhance the current of the molecular junctions. However, the OHP itself is not a suitable electrode material due to its poor conductivity.[39,40] Thus, it is better to use OHP as a light-absorbing layer and use another conductive material that is capable of effectively accommodating the photo-generated charges in the OHP. For this purpose, monolayer graphene, which has the advantage of the atomically

thin feature, allows photo-generated carriers to transit easily from the photo-active OHP layer to SAMs. In addition, the well-known electronic structure of graphene helps to analytically investigate the interfacial phenomena that occur when in contact with SAMs and OHPs.[41]

In this study, I implemented photo-modulated molecular junctions by employing an OHP/graphene heterostructure on SAMs. Through a single-source flash evaporation, I deposited the patterned and uniform methylammonium lead iodide (denoted as $MAPbI_3$) OHP film as a photo-active layer on the graphene. The electronic band properties of $MAPbI_3$/graphene interface were then investigated, and their response to light illumination was observed. To distinguish the role of SAM in the charge modulation, I fabricated two-terminal control devices without SAMs and quantitatively examined the electrical properties under dark and light illumination conditions. Then, I fabricated molecular junction devices with $MAPbI_3$/graphene/SAMs/Au structure to demonstrate the dependence of their charge transport modulation characteristics on light intensity. For further improvement in photocurrent to dark current ratio (PDR), I explored several molecules with different electric dipole moments to vary the $MAPbI_3$/graphene/SAM interface effect. Theoretical analysis based on Landauer formalism was performed to corroborate our experimental results and elucidate the role of SAMs and their interaction with $MAPbI_3$/graphene heterostructure.

2. Experiments and Results

2.1 Device Fabrication and Material Preparation

2.1.1 Device Configurations

In order to implement appropriate structure that fulfills sufficient light responsivity and device stability at the same time, vertical structure with light responsive layer of OHP deposited at the top of the conventional molecular device (graphene/SAM/Au) were designed as Figure 1a. Patterned holes and photoresist walls were made by conventional photolithography. Chemical vapor deposition (CVD)-grown monolayer graphene was transferred via wet transfer method. [42] The perovskite film was then deposited through the single-source evaporation method, as I previously reported. [43,44] Figure 1b shows images sequentially magnified from a whole substrate piece to a molecular junction from left to right in order: entire and enlarged optical microscope images of fabricated molecular junction devices on substrates, an atomic force microscope (AFM) image of a hole with a radius of 2 μm, and a cross-sectional transmission electron microscope (TEM) image of a molecular junction. The molecules used in this study are listed in Figure 1c. To achieve efficient charge transport modulation via electrode engineering, I selected several conjugated molecules rather than saturated molecules (e.g., alkanethiols) due to their relatively better conductivity, which originated from the small gap between the highest occupied molecular orbital (HOMO) and the lowest unoccupied molecular orbital (LUMO).[45-47] According to the direction of the intrinsic electric dipole moment, I used biphenyl-4-thiol (denoted as BPT), 1,4-benzenedithiol (BDT), and penta-fluoro-benzenenthiol (PFBT) in this study. BPT has an electric dipole oriented upwardly away from the thiol (-SH) group, whereas PFBT has an electric dipole in the opposite direction (i.e., toward the thiol group). BDT is considered to have the weakest electrical dipole moment due to its symmetric

structure. The monolayer graphene was characterized by measuring the Raman spectroscopy through the G and 2D peaks at energy shifts of 1580 and 2680 cm^{-1}, respectively (Figure 1d). As shown in Figure 1e, OHP has the crystal structure of ABX_3, where A is a small cation (e.g., methylammonium, denoted as MA), B is a metal ion (e.g., Pb^{2+} or Sn^{2+}), and X is a halide (e.g., I^-, Br^-, or Cl^-).

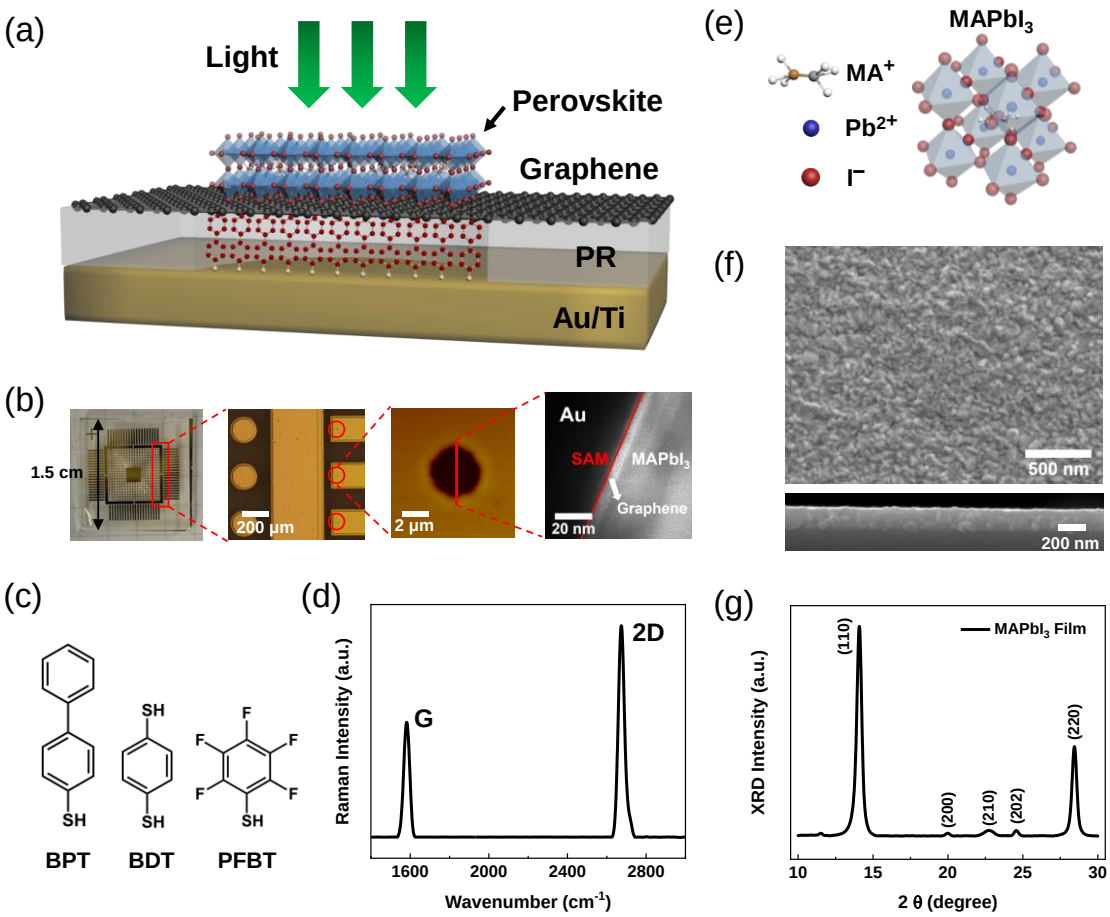

Figure 1. *(a) Schematic illustration of a fabricated molecular junction. (b) Optical, AFM, TEM images of the fabricated molecular devices. From left to right in order, entire and enlarged optical images of fabricated molecular junctions on substrates, AFM image of a hole, and cross-sectional TEM image of a molecular junction. (c) Molecules used in this study. From left to right in order, biphenyl-4-thiol (BPT), 1,4-benzenedithiol (BDT), and penta-fluoro-benzenenthiol (PFBT). (d) Raman spectrum of the monolayer graphene. (e) Schematic*

illustration of $MAPbI_3$. (f) Topological and cross-sectional FE-SEM images of the deposited $MAPbI_3$ film. (g) XRD spectrum of the deposited $MAPbI_3$ film.

2.1.2. Device Fabrication Procedure

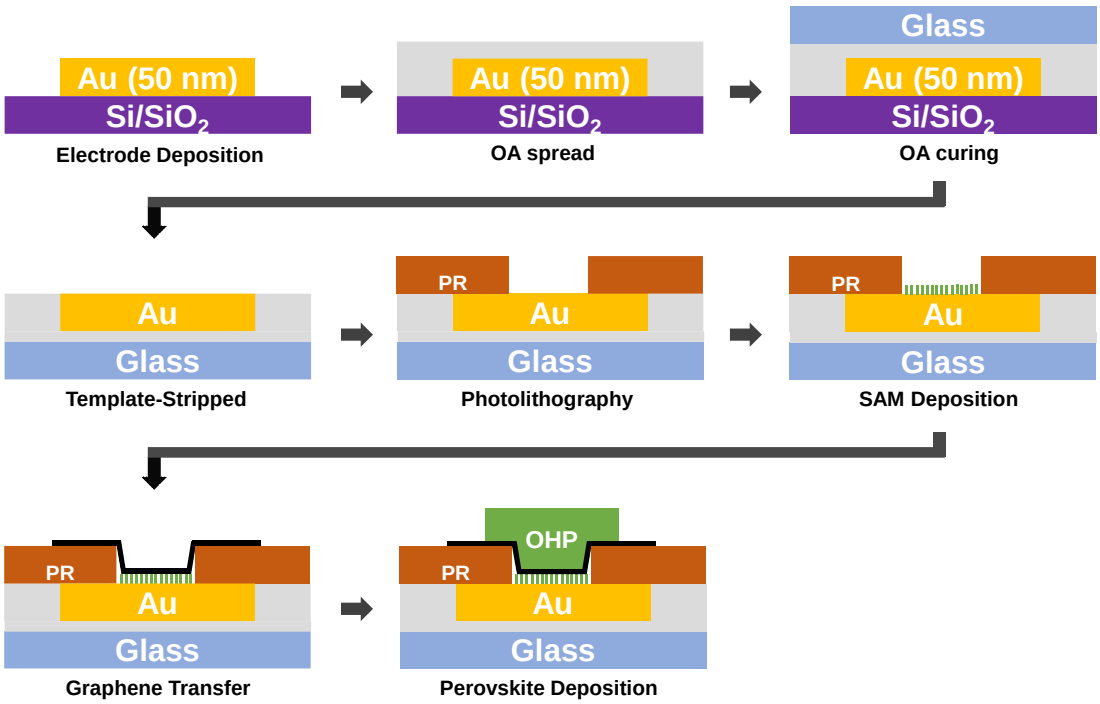

Figure 2. *Schematic images of the device fabrication process.*

Schematic images of the detailed fabrication process are provided in Figure 2. Since the yield of molecular devices is sensitive to the roughness of the bottom electrode, I used the template-stripped method to form ultra-flat surfaces. [74-75] Au bottom electrodes (50 nm thick) were deposited onto Si/SiO_2 substrates at the deposition rate of ~0.5 Å/s by using an electron-beam evaporator. Meanwhile, glass substrates were cleaned with acetone, isopropyl alcohol (IPA), and deionized (DI) water using a sonicator and then dried under a stream of N_2. The cleaned glass substrates were further treated with reactive ion etcher using O_2 gas (30 sccm, 50 W, 120 s) to remove remaining organic residues. After the cleaning process, a drop of optical adhesive (OA) (Norland, no.61) was applied onto the Au-deposited Si/SiO_2 substrates. Then, I

placed and pressed the cleaned glass substrates onto the applied OA to spread it evenly over each prepared Au film. All samples were exposed to ultraviolet (UV) light (1 h, 19.72 mW/cm^2) to cure the OA, using a UV-ozone cleaner (AH 1700, Ahtech LTS). Afterward, I split the glass/OA/Au layers from the Si/SiO_2 template by inserting a razor blade into the edge of the interface between the glass/OA/Au and the Si/SiO_2, carefully cleaving with gentle pressure. I made patterned device structures on these exposed surfaces by performing conventional photolithography and developing circular junctions with radii of 2 μm. I used a diluted photoresist (PR) (AZ 5214e) by mixing propylene glycol methyl ether acetate (PGMEA) at 1:1 ratio to lower the PR wall (height of ~250 nm), so that top graphene could better contact SAM. For the SAM formation, each sample was dipped into a 5 mM ethanol solution for 48 h in an N_2-filled glove box. Afterward, I gently rinsed the samples with anhydrous ethanol to wash out physisorbed molecules from SAMs. For the next step, monolayer graphene was transferred as a top electrode. Monolayer graphenes were purchased from Graphene Square Inc. For this process, a poly(methylmethacrylate) (PMMA) (MicroChem Corp.) layer was spin-coated onto the monolayer graphene film as a supporting layer. To etch the Cu foil, each sample was immersed in an ammonium persulfate aqueous solution for 1 h on a 90 ^{o}C hot plate. After the etching of the Cu foil, remaining graphene films were rinsed with DI water to remove the residual etchant. Then, the floating monolayer graphene films were transferred onto the sample. The supporting polymer was removed by soaking the samples in an acetone bath, then rinsing graphene with IPA. I used the single source flash evaporation method to deposit perovskite films onto the molecular devices. [43-44] The prepared $MAPbI_3$ and MAI powders (366 mg of $MAPbI_3$ and 99.96 mg of MAI) were loaded onto a tungsten boat in a vacuum chamber. The substrates were placed with shadow masks at the height of 30 cm away from the source material. Under the vacuum condition (10^{-6} Torr), the tungsten boat was rapidly heated by applying an abrupt high current of 100 A in 3 s so that the source powder could entirely be evaporated

within 30 s. In addition, since $MAPbI_3$ is easily degraded when exposed to ambient condition, I maintained every process involving $MAPbI_3$ from its deposition to electrical measurement to be conducted under vacuum condition, and samples were exposed to ambient only when transferring them from its production stage to measurement system.

2.1.3. OHP preparation

In several studies, OHP films were deposited on graphene through the spin-coating method.[48,49] However, it has been challenging to form a uniform, full-coverage OHP film using the typical solvents for OHP solutions such as dimethylformamide, dimethyl sulfoxide, and gamma-butyrolactone due to their polar characteristics.[50] Therefore, I used the single-source evaporation method to deposit a high-quality film of OHP with high uniformity and without pinholes, regardless of the surface energy on the substrate material.[43,44] First, $MAPbI_3$ powder, which can be used as the flash-evaporation source, was synthesized with high purity and characterized by powder X-ray diffraction (XRD) spectra (Figure 3). Field-emission scanning electron microscope (FE-SEM) images, shown in Figure 1f, confirmed that a pinhole-free and uniform MAPbI3 film with a film thickness of ~200 nm was formed by the flash evaporation (bottom image of Figure 1f). The quality of the deposited $MAPbI_3$ film was characterized by XRD (Figure 1g), absorbance, and AFM images (Figure 4), indicating that $MAPbI_3$ film was formed with good quality. In Figure 1g, large diffraction peaks of $MAPbI_3$ film were located at 14.08° and 28.44°, corresponding to the crystallographic planes (110) and (220), respectively. Minor peaks of the (200), (211), and (202) planes were also detected at 2θ values of 19.98°, 22.76°, and 24.58°, respectively. From the absorbance spectra of the $MAPbI_3$/graphene, the absorption edge was measured at 772 nm (optical bandgap ~1.6 eV), representing that $MAPbI_3$ on graphene absorbs over the entire visible-light range (Figure 4).

[51] The roughness of the deposited $MAPbI_3$ film was found to be ~3.3 nm through the AFM measurement (Figure 4).

Synthesis of perovskite powder: I synthesized $MAPbI_3$ single crystal powders as reported previously.[43-44] PbO powders, hydroiodic acid (HI, 57 wt% in H_2O), and hydrophosphorous acid (H_3PO_2, 50 w% in H_2O) were purchased from Sigma-Aldrich. Methylammonium iodide (MAI) was purchased from Greatcell Solar Materials Ltd. The perovskite powder was synthesized by the inverse temperature crystallization (ITC) method.[73] PbO (2.665 g) and MAI (1.898 g) powders were dissolved into a mixture containing 18 ml of HI and 2 ml of H_3PO_2. The mixed solution was heated to 120 ^oC on a hot plate with stirring until all the ingredients were dissolved. The solution was then cooled at room temperature. As the temperature of the solution decreased, $MAPbI_3$ powder was formed due to its decreasing solubility. After pouring the solution through Whatman filter papers, I collected and dried the synthesized $MAPbI_3$ powder in a vacuum desiccator overnight. Matching the calculated and experimental powder XRD data confirmed that a pure tetragonal phase of $MAPbI_3$ was obtained (Figure 3).

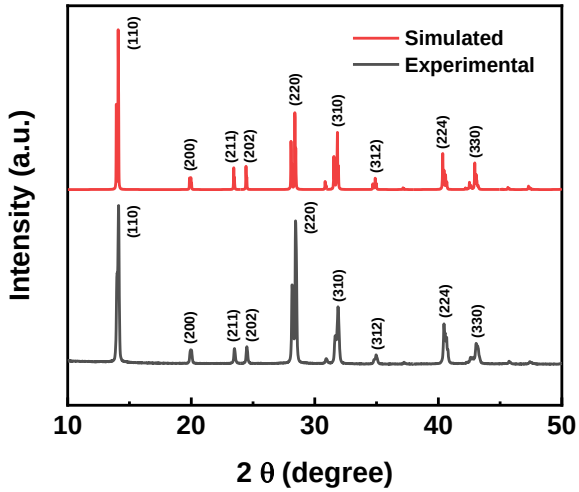

Figure 3. *shows the powder X-ray diffraction patterns for simulated and synthesized $MAPbI_3$ powder. The powder XRD spectra of the $MAPbI_3$ powder were well matched with the calculated*

XRD data (COD ID 2107954).[76]*Powder XRD spectra of simulated and synthesized $MAPbI_3$ powder.*

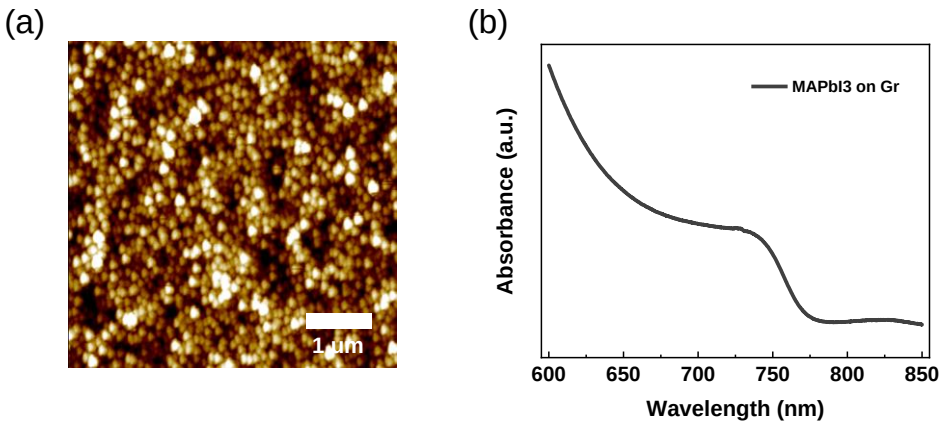

Figure 4. *shows the characterization of deposited $MAPbI_3$ film. The surface roughness was turned out to be ~3.3 nm. The absorption edge was estimated at ~772 nm (optical bandgap ~1.6 eV), which means that $MAPbI_3$/graphene absorbs the full visible range (400–700 nm).*[77] *(a) AFM image of deposited MAPbI3 film. (b) Absorbance spectra of deposited $MAPbI_3$ film.*

2.1.4. Characterization

The electrical characteristics of the molecular devices were determined by using a semiconductor parameter analyzer (Keithley 4200 SCS) and a probe station system (JANIS Model ST-500) under vacuum condition (~10^{-6} Torr). The light source was a 532 nm laser (Cobolt 04-01). Powder XRD and high-resolution XRD data were obtained by Rigaku SmartLab. FE-SEM images were collected with JSM-7800F Prime (JEOL Ltd) at an accelerating 5–10 kV voltage. Absorbance spectra were obtained using V-770 (Jasco). AFM and Kelvin probe force microscopy (KPFM) data were collected using NX-10 (Park Systems). Raman and PL spectra were measured by XperRAM 200 (Nanobase Inc.), and the time-resolved photoluminescence (TRPL) data was collected by XperRF (Nanobase Inc.). UPS

spectra were collected by using AXIS SUPRA (Kratos, U.K). FIB and TEM data were obtained by SMI3050SE (SII Nanotechnology) and Tecnai F20 (FEI).

2.2. Preliminary Studies: Photocurrent Characteristics of Composite Materials

2.2.1. Graphene/MaPbI3 Interfacial Band Structure at Light Illumination

Before investigating the molecular junctions, I examined, as a control group, the electrical properties of the $MAPbI_3$/graphene heterostructure in the absence of molecules and the light responsivity of the conventional Au/molecule/graphene vertical device. I used ultraviolet photoelectron spectroscopy (UPS) to verify the known work functions of monolayer graphene (~4.4 eV) and $MAPbI_3$ (~3.9 eV) (Figure 5a). [52,53] As depicted in Figure 5b, contact between $MAPbI_3$ and graphene initiates an internal electric field at the $MAPbI_3$/graphene interface due to the work function difference. Since the work function of the graphene is deeper than that of $MAPbI_3$, the energy band is bent down toward the $MAPbI_3$ direction. Under light illumination, electron-hole pairs are generated and form excitons in the $MAPbI_3$ film. Then, the charge carriers (electrons and holes) are separated from the photo-generated excitons and injected into graphene with the aid of the internal field at the $MAPbI_3$/graphene interface. This charge transfer phenomenon between the $MAPbI_3$ and graphene can be understood by observing the photoluminescence (PL) quenching phenomenon (Figure 5c). The PL peak positions of both $MAPbI_3$ film and $MAPbI_3$/graphene heterostructure are located around ~770 nm, which corresponds to the band-to-band transition peak of ~1.6 eV, similar to the previously reported values.[51] Without the PL peak shift, the maximal PL intensity of the $MAPbI_3$/graphene was quenched by 55% compared to that of pristine $MAPbI_3$ film. This PL quenching phenomenon represents the effective charge transfer between the $MAPbI_3$ and graphene, resulting from the internal field at the interface and π–π interaction between sp^2 hybridized graphene and $MAPbI_3$.[48, 54]

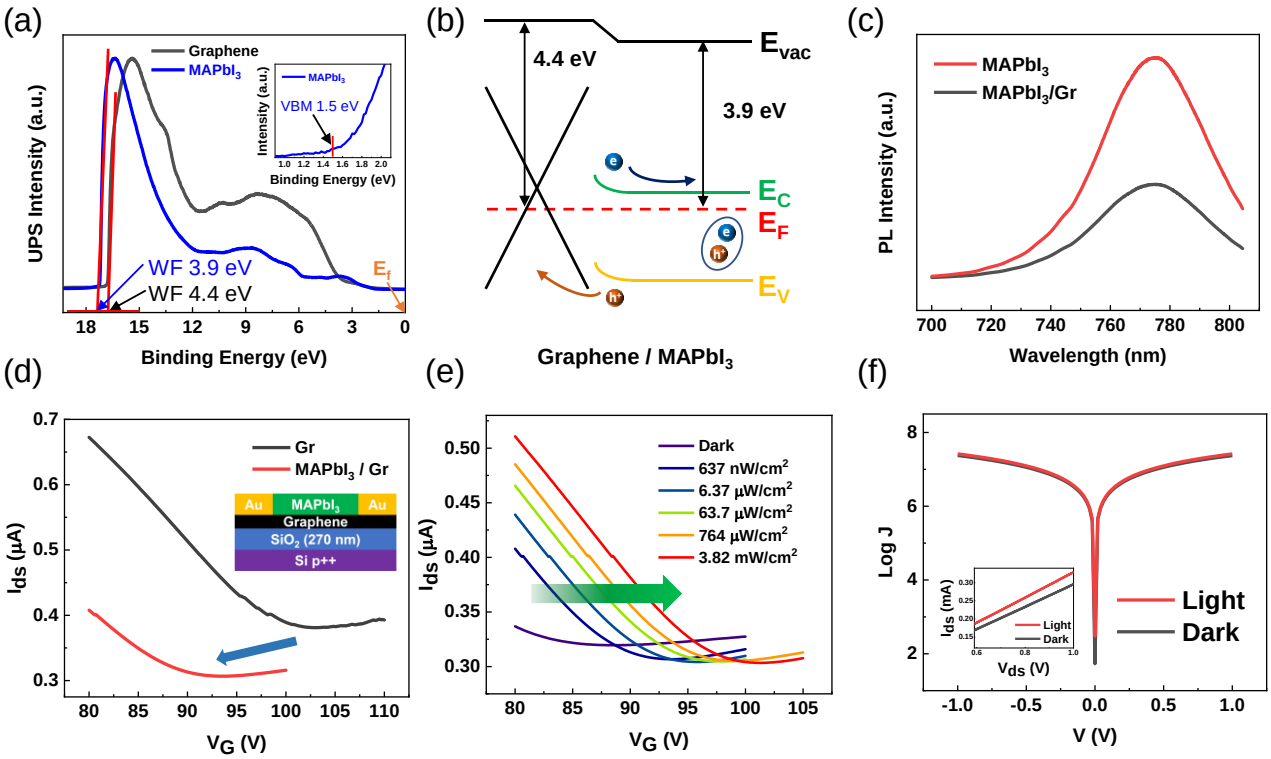

Figure 5. *(a) UPS spectra of the $MAPbI_3$ film using the single-source flash evaporation method and the monolayer graphene. (b) Energy band diagram when the graphene and $MAPbI_3$ form a contact. (c) PL spectra of the pristine $MAPbI_3$ film and $MAPbI_3$/graphene heterostructure upon 532 nm excitation. (d) I_{ds}–V_{gs} characteristics of a pristine GFET (denoted as Gr, black curve) and $MAPbI_3$/graphene hybrid FET (denoted as $MAPbI_3$/Gr, red curve). The inset shows the schematic image of a $MAPbI_3$/Gr FET device. (e) I_{ds}–V_{gs} curves of a $MAPbI_3$/Gr FET showing a gradual p-doping effect as the light intensity increases. (f) Electrical characteristics of a control device ($MAPbI_3$/graphene/Au without SAM) under the light intensity of 3.82 mW/cm^2. The left inset shows the I–V curve on linear scale and the right inset presents the schematic image of the fabricated control device*

To directly verify the charge transfer from perovskite to graphene, I fabricated a graphene field-effect transistor (GFET) covered with the $MAPbI_3$ film as a light harvester and estimated how many photo-generated carriers were transferred and contributed to the photocurrent. As

mentioned above, the electron transfer from $MAPbI_3$ to graphene due to the work function mismatch causes initial n-doping of the monolayer graphene (Figure 5d). When the light is illuminated, photo-generated hole injection at the $MAPbI_3$/graphene interface promotes the gradual p-type doping of graphene (Figure 5e). The increase in the number of charge carriers in graphene with increasing light intensity can be calculated from the Dirac voltage values obtained experimentally, according to the following relations.[55,56]

$$V_{gs} - V_{Dirac} = \frac{E_f}{e} + \frac{e\triangle n}{C_{ox}} \quad (1)$$

$$\Delta n = \Delta(n_e - p_h) = \frac{2}{\pi}\left(\frac{k_B T}{\hbar v_f}\right)^2 \{F_1(+\xi) - F_1(-\xi)\} \quad (2)$$

where e is the elementary charge, C_{ox} is the gate oxide capacitance per unit area, n_e and p_h are electron and hole densities, respectively, k_B is the Boltzmann constant, T is the temperature, $\hbar$ is the reduced Planck constant, v_f is the Fermi velocity of graphene (~10^6 m/s), $F_1(\eta)$ is Fermi-Dirac integral $F_j(\eta)$ with j = 1, $\xi = \frac{\Delta E}{kT}$, and ΔE is the energy difference between the Dirac point and the Fermi level of graphene.

The detailed calculation process and the logic I used to deduce the interfacial band property quantitatively is described in Section 3.2. Briefly, Equations (1) and (2) can be combined to extract the value of $\Delta n = 11.5 \times 10^{11}$ cm^{-2} under a light intensity of 3.82 mW/cm^2. Given the intrinsic carrier concentration of graphene (~9×10^{12} cm^{-2}),[57] the number of carriers in the monolayer graphene channel increased by ~13 % with respect to the intrinsic carrier concentration under a light intensity of 3.82 mW/cm^2. In this manner, I measured the current-voltage (I−V) characteristics of a two-terminal control device ($MAPbI_3$/graphene/Au without

SAM) under dark and illuminated conditions. Even with a high-intensity illumination (3.82 mW/cm^2) of 532 nm laser, the current enhancement due to the photocurrent generation was rather modest, exhibiting an increase of about 15 % with respect to the dark current (see Figure 5f). The consistency of this result with the ~13 % increase of carrier concentration derived from GFET measurement under the same light intensity supports our argument.

2.2.2. Calculation of transferred carriers in $MAPbI_3$/graphene heterostructure.

I transferred graphene on the Si substrate with 270 nm SiO_2 to make a graphene FET structure. In the graphene FET (GFET), the p-doped graphene band was drawn down until the Dirac point reached the Fermi level (Figure 6) by applying a sufficient positive back gate voltage (also known as Dirac voltage). Since the Dirac voltage entirely alleviates the hole doping in graphene, the minimum current in the transfer curve occurs when Dirac voltage is applied (see Figure 5d). For the same reason, the magnitude of the Dirac voltage is proportional to the original doping level. In this manner, by analyzing the lateral shift of transfer curve minimum upon external perturbation (see the green arrow of Figure 5e), I can estimate the amount of additional doping level in the graphene. Consequently, from the transfer curves obtained of the light illuminated GFET, I numerically calculated the amount of transferred photo-generated carriers from $MAPbI_3$ to graphene.

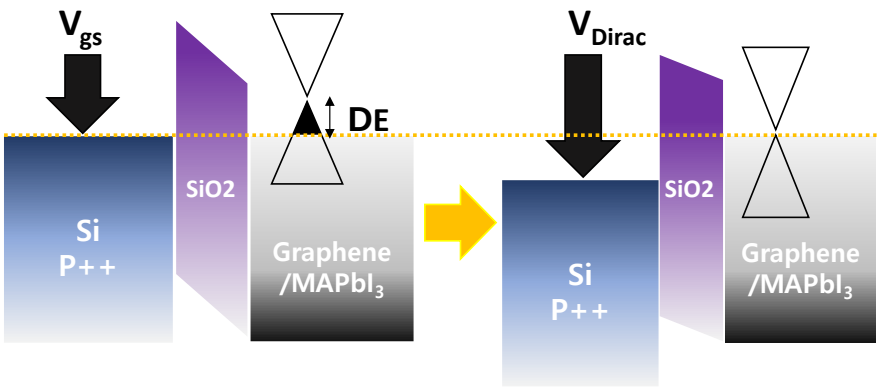

Figure 6. *Band diagram of GFET at the zero gate voltage (left) and the Dirac voltage (right)*

Since the gate voltage (V_{gs}) in GFET compensates not only the graphene band shift (ϕ_{gr}) but also the internal field at the oxide layer (ϕ_{ox}), the applied V_{gs} can be expressed as the sum of ϕ_{ox} and ϕ_{gr}. For ϕ_{gr}, it can be replaced by $\Delta E = E_{dp} - E_f$, where E_{dp} is the energy level of Dirac point with respect to the vacuum level and E_f is the Fermi level of the graphene. By regarding Si/SiO_2/graphene configuration as a capacitor structure, as shown in Figure 6, ϕ_{ox} can be expressed in terms of charge carrier accumulation (n) at the interfaces. Thereby, V_{gs} can be expressed as Equation 3, [78,79]

$$V_{gs} - V_{Dirac} = \phi_{ox} + \phi_{gr} = \frac{e\Delta n}{C_{ox}} + \left(E_{dp} - E_f\right)/e \qquad (3)$$

where e is the elementary charge, C_{ox} is the gate oxide capacitance per unit area, V_{Dirac} is the Dirac voltage. On the other hand, if I assume that carrier accumulation is equal to excessive charge doped in graphene, Δn can be directly calculated in terms of ΔE with the aid of well-known density of state (DOS) of pristine monolayer graphene, $E/\hbar v_f$, where $\hbar$ is the Planck constant divided by 2π, v_f is the Fermi velocity of graphene (~10^6 m/s). Therefore, ϕ_{ox} can be expressed in terms of ΔE as given in Equation 4,[79,80] and eventually V_{gs} becomes a function of ΔE.

$$\triangle \phi_{ox} = \frac{e\Delta n}{C_{ox}} = \frac{e}{C_{ox}} \triangle (n_e - p_h) = \frac{2e}{\pi C_{ox}} \left(\frac{k_B T}{\hbar v_f}\right)^2 \{F_1(+\xi) - F_1(-\xi)\}$$

$$= \frac{2e}{\pi C_{ox} (\hbar v_f)^2} \{\int_0^{\infty} \frac{E}{\exp^{[E-\Delta E]/kT}+1} dE - \int_0^{-\infty} \frac{E}{\exp^{-[E-\Delta E]/kT}+1} dE\} \qquad (4)$$

where n_e and p_h are electron and hole densities, respectively, k_B is the Boltzman constant, T is the temperature, $F_1(\eta)$ is is Fermi-Dirac integral $F_j(\eta)$ with j = 1, $\xi = \frac{\Delta E}{kT}$.

Table 1. *Experimentally obtained Dirac voltages, ΔE values extracted by inserting V_{Dirac}, and calculated carrier concentrations by illumination.*

Intensity	Dark	637 (nW/cm^2)	6.37 (μW/cm^2)	63.7 (μW/cm^2)	764 (μW/cm^2)	3.82 (mW/cm^2)
V_{dirac} (V)	87	93	95	98	100	103
$E_{dp}-E_f$ (eV)	0.302	0.311	0.314	0.318	0.321	0.324
Increased carrier n ($\times 10^{11}$ cm^{-2})	0	4.10	6.16	7.79	9.02	11.5

I substituted V_{gs} from Equation 3 with the zero and solved the ΔE_0 (initial ΔE) value, which implies the original doping level of graphene before the gate voltage was ever applied. Then I substituted this value into Equation 4 again to obtain carrier density n. For GFET covered with $MAPbI_3$ film, I obtained transfer curves for various intensities of light illumination from the dark condition to 3.82 mW/cm^2 (see Figure 5e). I observed larger V_{Dirac} values under higher light intensities, as more photo-generated charges transferred from $MAPbI_3$ induced heavier p-type doping in graphene. Based on the method from the preceding paragraph, I substitute experimentally obtained Dirac voltage into Equation 3 to calculate the doping level of graphene ($\sim\Delta E_0$) and the graphene carrier densities (n) under each light intensity. To quantify the effect of photo-induced doping upon light intensity, I evaluate the increment of carriers by subtracting carrier density measured in the dark condition (see Table 1). Increased carrier concentration in total at highest light intensity was $\Delta n \sim 11.5 \times 10^{11}$ cm^{-2}. Comparing this to the conventionally known carrier concentration of graphene ($\sim 0.9 \times 10^{13}$ cm^{-2}), I could expect about ~13% increase of current density under 3.82 mW/cm^{-2} light irradiation. This current

increase rate coincides with ~15% of the control experiment (see Figure 5f), which used the same device structure of the main experiment only without molecules (Au/Graphene/$MAPbI_3$)

2.2.3. Controlled experiment of Au/PFBT/graphene junctions without $MAPbI_3$

In the presence of light, the metal electrodes also generate hot carriers, which also enhance electrical transport. By conducting control experiments to prove that the current enhancement originates from the heterostructure electrode but not Au, I could exclude the influence of such effect. I compared the properties of Au/PFBT/graphene junctions without and with MAPbI3 Unlike the device with a perovskite layer, where photocurrent enhancement was up to several 100% (see Figure 8), those without the MAPbI3 layer (i.e. the control device) have shown a minute increase of about ~17% in average. Statistical data of both Figure 6 (a) and (b) support that the light responsivity of the gold-molecule-graphene junction is fairly weak and negligible in our main results.

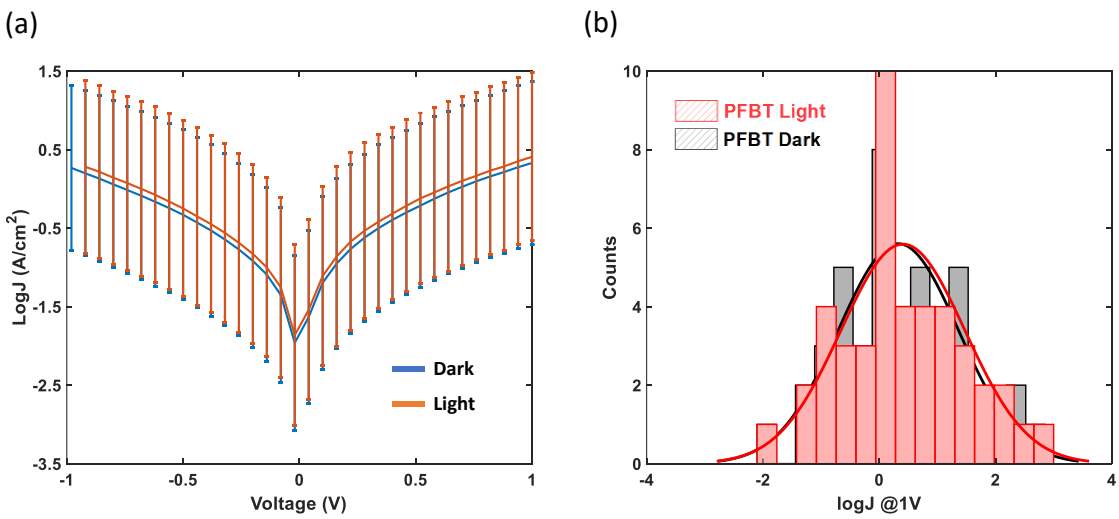

Figure 6. (*a) The logarithmic average current densities according to the voltage for PFBT. Blue and orange lines represent the dark current and photocurrent, respectively. (b) Statistical data and its Gaussian fitting of logarithmic current densities of all Au/PFBT/Graphene molecular junctions under the dark(black) and light-illuminated (red) conditions. They were measured before MaPbI3 being deposited above*

2.3. Realization of Photo-Switchable Molecular Device

2.3.1. Photoresponsive electrical property of the Au/PFBT/graphene/$MAPbI_3$ Structure

The first reversible light-responding device stable enough to pass the dozen trials were earned in the case of Biphenyl thiol SAM junction. Figure 7 shows the electrical characteristics of $MAPbI_3$/graphene/BPT/Au molecular junctions according to the intensity of the illuminated light. The BPT molecules were adopted for its conductive nature originated from delocalized π-electrons.[58] As shown in Figure 7a, reversible and light intensity-dependent photocurrent modulation was observed for BPT molecular junctions. Specifically, the current increased about ~250 % at 1 V under the highest light intensity (637 μW/cm^2), compared to the dark condition. Figures 3b and 3c show the statistical analysis for the BPT molecular junctions. I plotted the histograms of the logarithmic current density (Log J) at 1 V of all working BPT molecular junctions and then performed Gaussian fittings on the histograms. Extracted average logarithmic current densities were found to be ~3.04 (~1.10×10^3 A/cm^2 at 1 V) for the dark condition (Gaussian standard deviation σ of ~0.33) and ~3.20 (~1.59×10^3 A/cm^2 at 1 V) under the light illumination (σ of ~0.43), corresponding to ~145 % photo-induced current enhancement. Note that PDR of BPT molecular junctions outperforms that of the control device without SAM (~15%) by an order of magnitude. Such a significant difference between the systems with and without molecules implies that SAM plays an essential role in the photoinduced current enhancement, as discussed later.

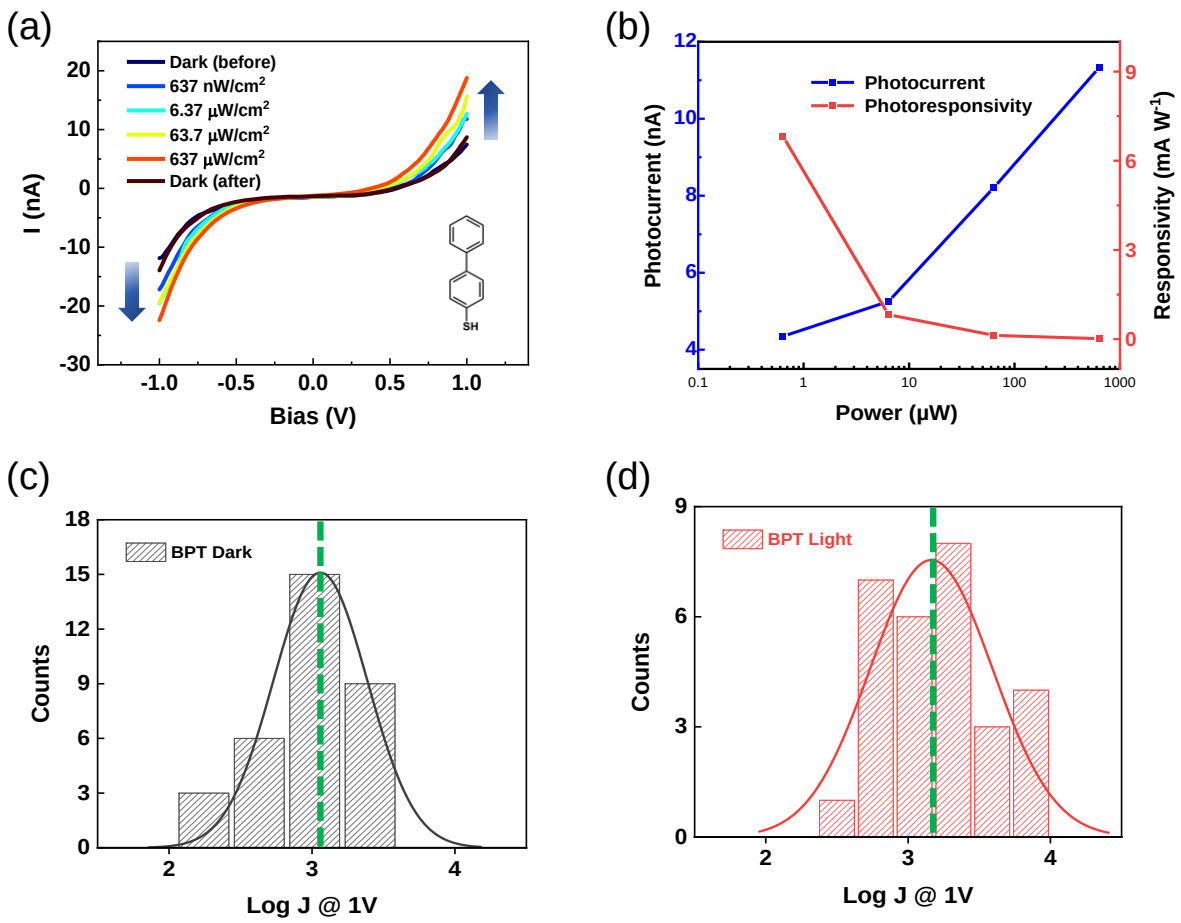

Figure 7. *(a) I–V characteristics of the representative BPT-based molecular junction according to the light intensity. (b) Photocurrent (= current when illuminated – current at dark condition) and photo responsivity data plot of Au/BPT/Graphene/MAPbI$_3$ junction. (c, d) Statistical data with Gaussian fitting of logarithmic current densities of all BPT molecular junctions under the (c) dark and (d) light conditions. The mean logarithmic current densities at 1 V were represented as green dashed lines.*

2.3.2. Statistical data of BDT and PFBT-based molecular junctions

After the experiments on BPT SAM device, I expanded the photocurrent measurement to the case of BDT and PFBT molecule. Figure 8 demonstrates statistical data of BDT and PFBT-based molecular junctions at 1 V. Under the dark condition, average logarithmic current

densities (Log J) of BDT and PFBT were 2.63 and 3.86, respectively. With the light illumination, the Log J values of BDT and PFBT were 2.98 and 4.52, corresponding to ~223 % current enhancement for BDT and ~ 450% for PFBT.

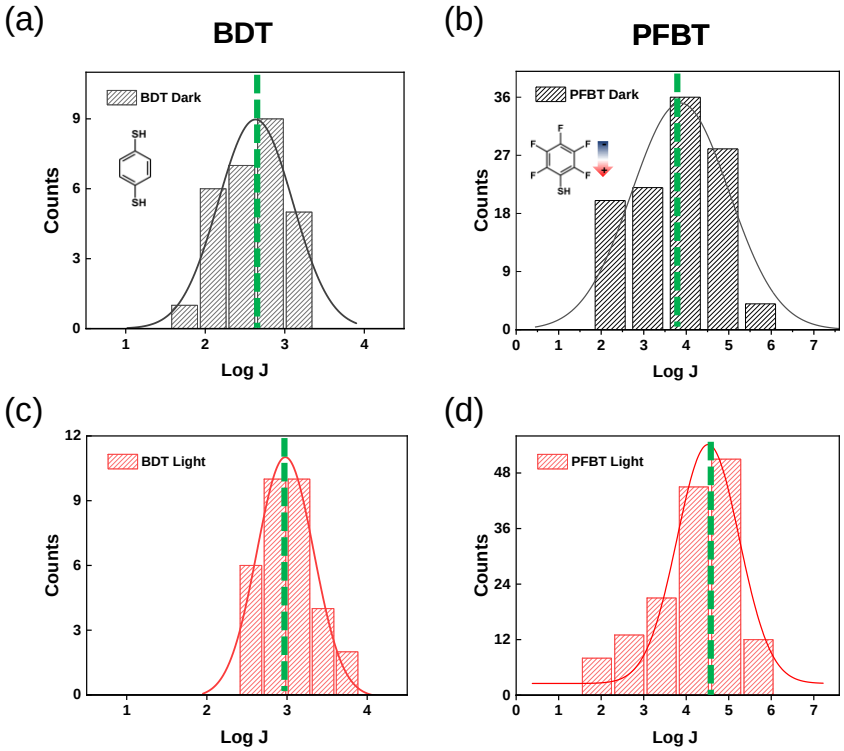

Figure 8. *Statistical data of (a, c) BDT and (b, d) PFBT-based molecular junctions at 1 V. Figure S11 represents statistical data of all molecular junctions at the bias of -1V. Under the dark condition, average logarithmic current densities (Log J) were 3.21 for BPT, 3.19 for BDT, and 3.73 for PFBT, respectively. With the light illumination, the Log J values were 3.3 for BTP, 3.3 for BDT, and 4.44 for PFBT, corresponding to ~123 % current enhancement for BDT, ~128 % for BDT, and ~513 % for PFBT.*

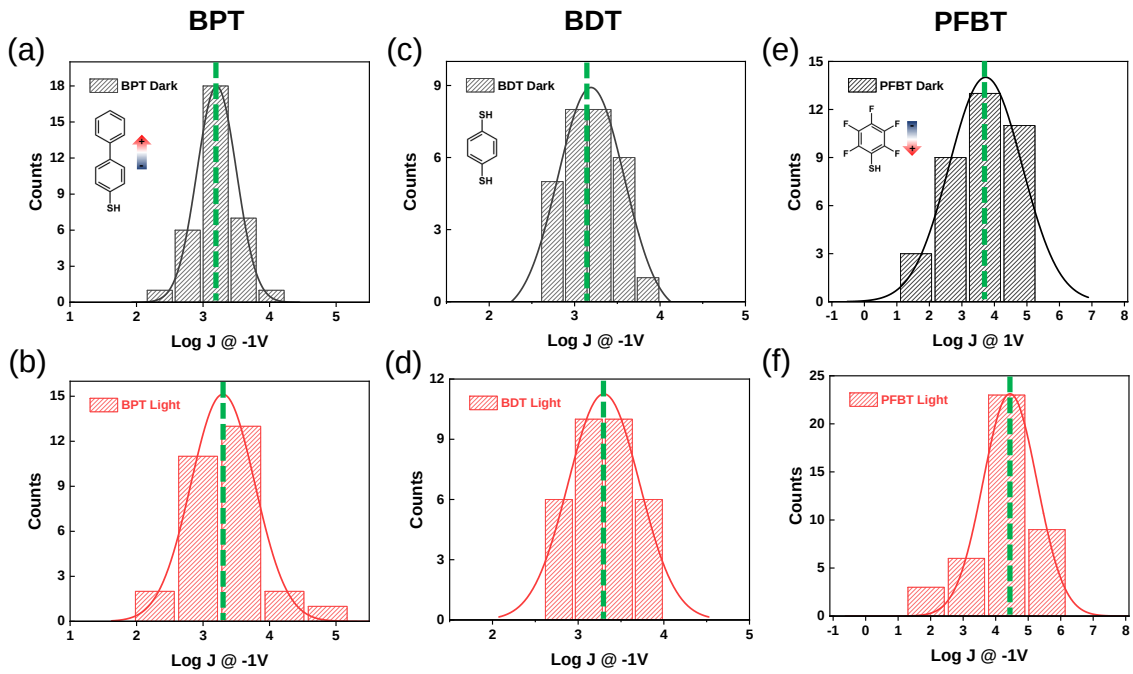

Figure 9. *Statistical data of (a, b) BPT, (c, d) BDT, and (e, f) PFBT-based molecular junctions at -1V.*

2.3.3. Switching characteristics of the representative BPT, BDT, PFBT molecular junction

To demonstrates the reversible nature of the light responses in the given devices, I measured the in-situ photocurrent switching. Figure 10 shows the switching behavior of the representative BPT (Figure 10a), BDT (Figure 10b), and PFBT molecular junction (Figures 10c and 10d). The rise and decay times of the molecular junctions (shaded regions in Figures 10a, 10b, and 10c) were found to be ~3.1 s and ~2.0 s for BPT, ~0.1 s and ~0.3 s for BDT, and ~3.1 s and ~2.0 s for PFBT junctions, respectively. These switching times are faster than other molecular devices using photo-switchable molecules such as diarylethene or aryl-azobenzene of which switching time exceeds 10 minutes.[S6-S8] In addition, we performed multiple-cycle switching measurements for a PFBT molecular junction, as shown in Figure 10d.

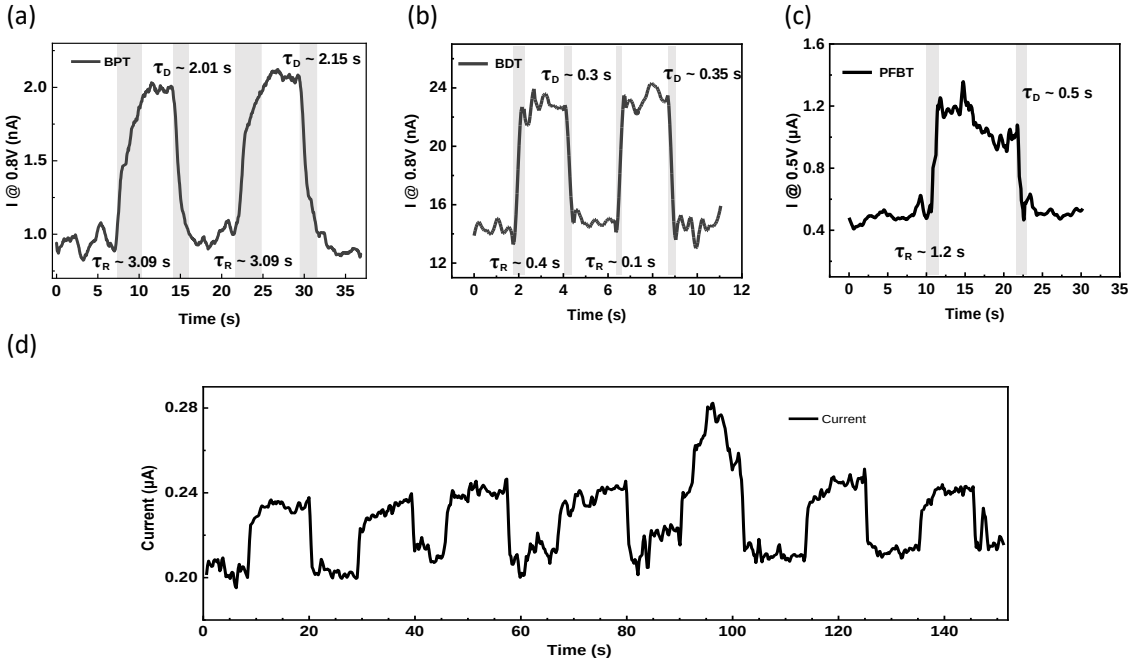

Figure 10. *Switching characteristics of (a) BPT (measured at 0.8 V), (b) BDT (at 0.8 V), and (c) PFBT (at 0.5 V) molecular junctions under light intensity of 0.64 mW/cm^2. (d) Multiple switching characteristics of a PFBT junction measured at 0.25 V under light intensity of 64 μW/cm^2.*

2.3.4. Influence of Molecular Dipole Variations on Photocurrent Traits

However, this current enhancement of BPT molecular junctions is somewhat smaller than the previous results using photo-stimulated molecules such as diarylethene or azobenzene which have shown increases about an order of magnitude.[30, 33-35] In such context, for further improvement in current enhancement at molecular junctions, I chose to vary the molecular dipole moment. Effect of dipoles on the transport characteristics had often considered to be elusive, due to depolarizations by disorders or interactions that occur among the molecules in SAM layer. However, depolarization effect did not appear to be dominant in our study in which the transport properties showed a clear dipole dependence probably due to a low packing density of phenyl-based molecule SAMs.[59, 60] Moreover, a series of recent studies[61, 62] have

reported a critical role of dipoles in the charge transport behaviors in large area molecular junctions, which supports that the depolarization effect can be neglected in these junctions.

BPT has an intrinsic dipole moment, oriented from the thiol group (δ^-) to the molecular backbone (δ^+). Since the injected holes from $MAPbI_3$ are major carriers of the photocurrent, the δ^+ partial charge at the side of BPT SAM hinders the charge transport of injected holes (Figure 4a). Hence, adjusting the direction of molecular dipole moments to facilitate hole injection would be expected to boost photo-induced current enhancement. For this purpose, I used BDT and PFBT molecules in addition to BPT. BDT has no intrinsic dipole due to its symmetric structure, and PFBT has a dipole moment in the direction opposite that of BPT, i.e., oriented from the molecular backbone (δ^-) to the thiol group (δ^+).[63] The dipole moment of each molecule, as obtained through density functional theory (DFT) calculation, was ~1.01 D for BPT, 0.00 D for BDT, and 1.55 D for PFBT (see Table 2).

The interruption of hole injection by dipole-induced field can be eliminated in the case of BDT, and the δ^- partial charge of PFBT SAM can provoke the injection of photo-generated holes from the $MAPbI_3$ film to molecular junctions (Figure 11b). Figures 11c and 11d show the average logarithmic current densities of BDT and PFBT molecular junctions, respectively. On average, PDR of 220% and 450% were obtained for BDT (Figure 11c) and PFBT (Figure 11d) molecular junctions, respectively. Especially, a ~1000 % current increase was observed for the best-performing PFBT molecular device. I used PL quenching and time-resolved photoluminescence (TRPL) spectra to corroborate this molecular dipole direction effect on performance behavior. Figure 11e shows the PL spectra of $MAPbI_3$/graphene/SAM/Au junctions for all molecules used in this study. The PL intensity decreased the most in the PFBT case and the least in the BPT case. The stronger the δ^- partial charges on the graphene side of the molecular dipole, the greater the PL intensity reduction due to the improved hole injection. In Figures 11e and 11f, 'Without SAM' refers to the $MAPbI_3$/graphene/Au junction

lacking SAM. Figure 11f shows the TRPL spectra of $MAPbI_3$/graphene/SAM/Au junctions. Average carrier lifetimes, extracted via conventional biexponential fitting to TRPL curves, were as follows: ~5.9 ns for BPT, 3.0 ns for BDT, 2.6 ns for 'Without SAM', and 1.8 ns for PFBT. In agreement with the PL quenching and electrical data, the carrier lifetime decreased sequentially from BPT to PFBT as the strength of the dipole-assisted hole injection effect increased, again suggesting enhanced charge extraction from BPT to PFBT.

Table 2. *Dipole moments and HOMO-LUMO gap of all molecule calculated by DFT. Dipole moments and HOMO–LUMO gap of all molecules in the gas phase were calculated using density functional theory (DFT). All calculations were performed with the ORCA code.*[84] *B3LYP functional with a quadruple-zeta Ahlrichs basis set (def2-QZVP) was used for all atoms.*[85] *RIJCOSX scheme was used to accelerate the calculation of integrals with the J auxiliary basis set by Weigend (def2/J).* [86, 87] *The molecular geometries were first allowed to relax under neutral conditions with a self-consistent cycle energy convergence limit of* 10^{-8} *Hartrees and a maximum force gradient of* 3×10^{-4} *Hartree/Bohr. The ionization potential (corresponding to the HOMO level from vacuum) was then calculated by the delta-SCF procedure; values for the electron affinity (LUMO level from vacuum) was obtained by adding the energy of the first excited state (HOMO–LUMO gap) which was estimated from time-dependent density functional theory calculations.*

	BPT	**BDT**	**PFBT**
Dipole moment (D)	1.01	0.00	1.55
HOMO–LUMO gap (eV)	3.34	3.48	3.82

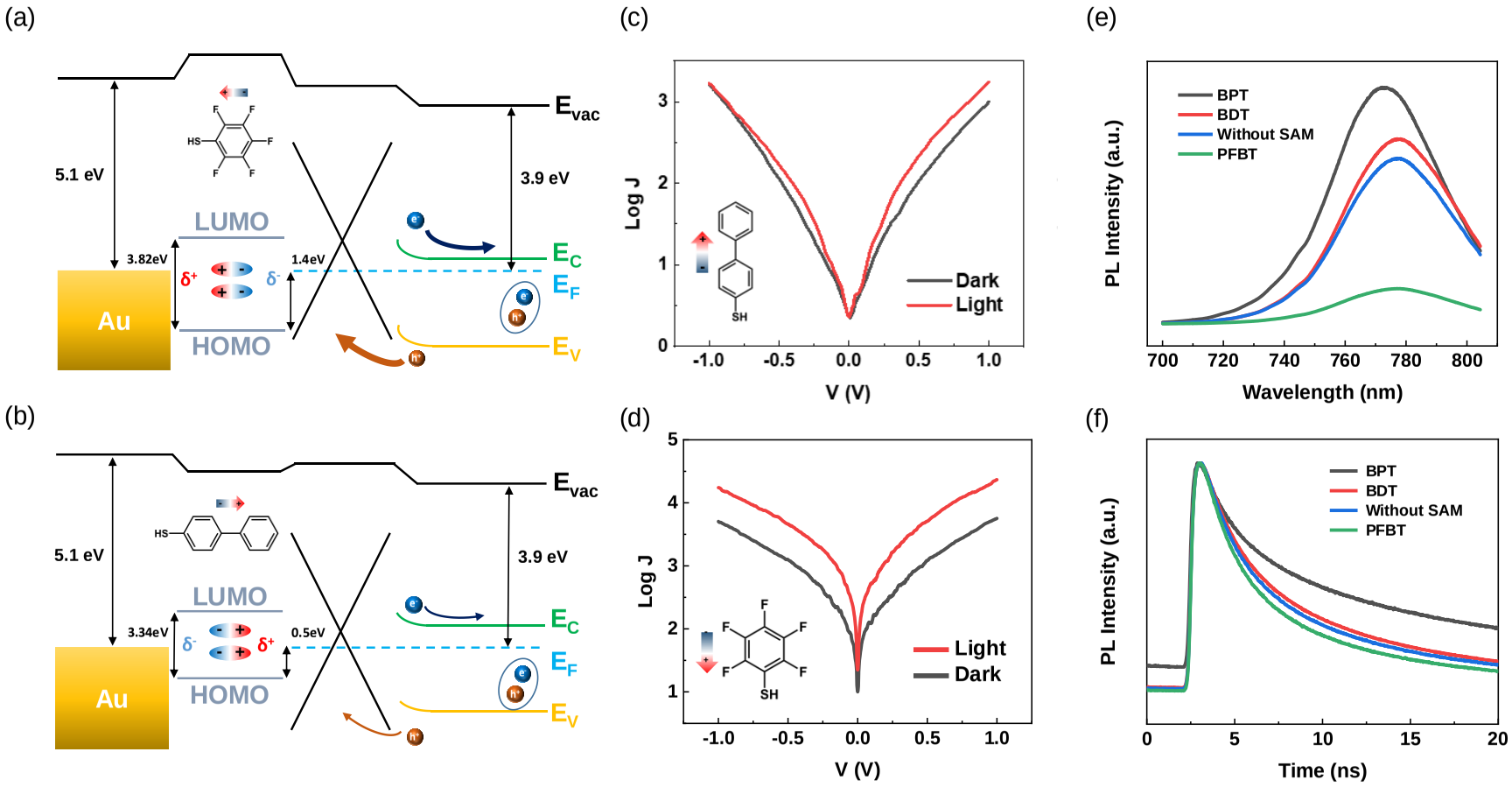
(a)
5.1 eV
3.9 eV
LUMO
HOMO
3.82eV
1.4eV
Au
E_{vac}
E_C
E_F
E_V
(b)
5.1 eV
3.9 eV
LUMO
HOMO
3.34eV
0.5eV
Au
E_{vac}
E_C
E_F
E_V
(c)
Log J
V (V)
Dark
Light
(d)
Log J
V (V)
Light
Dark
(e)
PL Intensity (a.u.)
Wavelength (nm)
BPT
BDT
Without SAM
PFBT
(f)
PL Intensity (a.u.)
Time (ns)
BPT
BDT
Without SAM
PFBT

Figure 11. *Photo-induced current enhancement by dipole-induced field variation. (a, b) Schematic mechanism of photo-induced current enhancement by variating dipole moments. Band diagrams of (a) BPT-based and (b) PFBT-based molecular junction. (c, d) Logarithmic average current densities according to the voltage for (c) BDT and (d) PFBT molecular junctions. Red and black lines represent the photocurrent and dark current, respectively. (e) PL quenching characteristics according to the dipole direction. (f) TRPL spectra of perovskite/graphene/SAM structure according to the dipole moment variation.*

2.3.5. UPS and KPM data of Au films with SAMs

Additional data of KPM and UPS supported my claim regarding the band configurations. Figure 12 shows the UPS spectra of SAM-treated Au films. Generally, a potential shift of metal is induced when a polar SAM is formed, which can be observed as a work function shift in the SAM-treated metal. To be specific, dipoles with the direction oriented from the metal surface ($\boldsymbol{\delta^-}$) to the molecular backbone ($\boldsymbol{\delta^+}$) decrease the gold work function (BPT in this study), whereas dipoles with the opposite direction increase it (PFBT in this study). Known values for modified work functions with BPT and PFBT are 4.5 and 5.5 eV, respectively, [88, 89] which is verified by UPS (Figure 12) and Kelvin Probe Force Microscopy (KPFM, Figure 13).

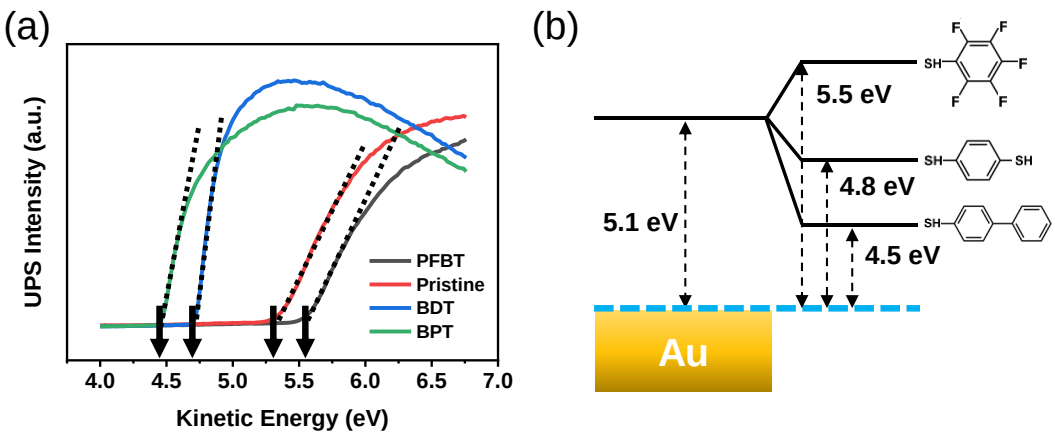

Figure 12. *(a) UPS data of SAM-treated Au films. (b) Schematic band diagram for SAM-treated Au films.*

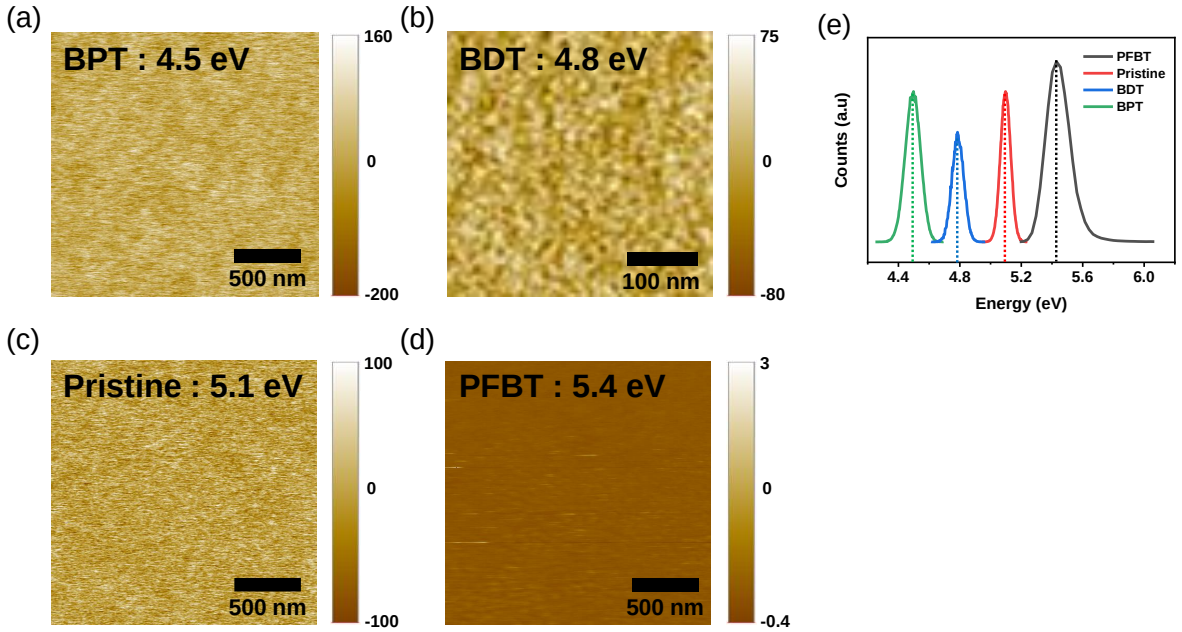

Figure 13. *KPFM data of (a) BPT-treated, (b) BDT-treated, (c) pristine, (d) PFBT-treated Au films. (e) Pixel analysis for all SAM-modified Au films.*

3. Analysis and Discussion

3.1. Background for Theoretical Analysis on Charge Transport of Molecular Junction

To elucidate the role of SAM on the photoinduced current enhancement of molecular junctions, I applied Landauer formalism to the obtained electrical data. In the case of conventional molecules with a large HOMO-LUMO gap (e.g., alkanethiols), where the frontier orbital level is sufficiently far from the Fermi level, non-resonant direct tunneling governs the charge transport, which is usually described by simplified Simmons model.[64] Indeed, the transport in our octanedithiol devices can be well described by Simmon's model and they exhibited the photoinduced current enhancement of approximately 11% (see Figure 14).

The electron transport through a molecule placed between Au and graphene can be treated as simple tunneling through a potential barrier when the molecular orbital level is sufficiently far from Fermi level, under a given bias voltage. From this point of view, WKB approximation can be applied to obtain Simmon's theory where the current density J is expressed as J ~ $exp(-\beta d)$, where $\beta \sim 4\pi\sqrt{2m(\bar{\varphi})}/h$, $\bar{\varphi}$ is the mean barrier height, m is the effective mass of carriers, and d is the tunneling length (the length of the molecule).[90] On the other hand, as already introduced in the main text, the photo-induced current enhancement in our vertical control device without molecules is simply dependent on the increment of charge carriers in horizontal graphene sheets. Integrating these, I can predict the photo-response of the I–V characteristics in the Au/SAM/Gr/$MAPbI_3$ heterostructure. In such device structure with a constant z-direction tunneling probability (~ $exp(-\beta d)$) , the photo-induced current modulation would be influenced mostly by the change of graphene carrier concentration. I corroborated this in the octanedithiol (C8) molecular junction, by showing that its PDR of ~11% at 3.82 mW/cm^2 light irradiation (Figure 14) is comparable to a ~13% increase in charge

concentration calculated in the previous section, and a ~15% increase in the control device (see Figure 15).

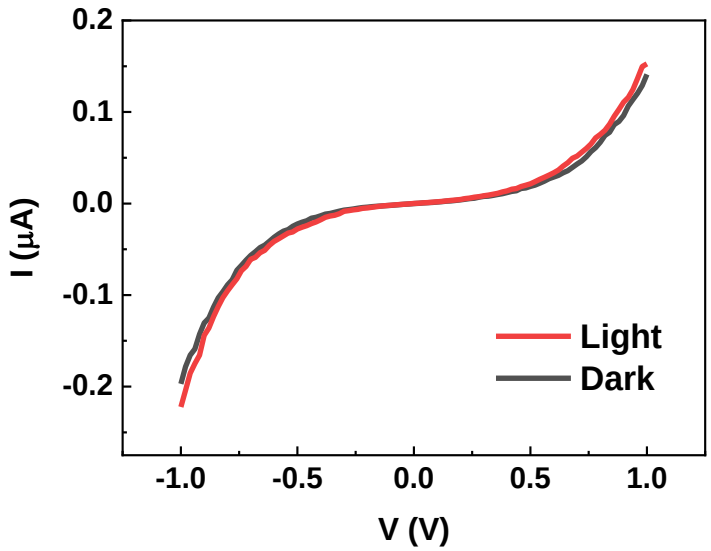

Figure 14. *I–V characteristics of a C8-based molecular junction.*

On the other hand, in the case of devices with phenyl ring-based SAM, current increases of several hundred percent occurred as suggested previously through experimental data, which is about ten times larger than that of the alkanethiol chains or controlled experiment. The simple direct tunneling model is unsuitable for justifying a significantly large photo-induced current enhancement in π-conjugated molecular junction devices. I deduced that such result occurred as the primary transport mechanism of phenyl ring-based molecular junctions is resonant tunneling. Unlike the alkyl chain case, since the HOMO level of the phenyl-ring-based conjugated molecules used in our study is comparatively close to the electrode's Fermi level, the resonant tunneling model is more relevant and useful than the Simmons model. [65] Under the additional assumption that electrons are transported coherently, the general equation describing resonant tunneling current can be given as the following equations. [91]

$$I(V_{bias}) = \int_{-\infty}^{\infty} dE\, T(E)\left(f(E,\mu) - f(E,\mu + eV_{bias})\right) \quad (78)$$

$$T(E) = \sum_n \frac{4\Gamma_B\,\Gamma_T}{((\Gamma_B+\Gamma_T)^2+(E-E_n)^2)} \approx \frac{4\Gamma_B\,\Gamma_T}{((\Gamma_B+\Gamma_T)^2+(E-E_0)^2)} \quad (79)$$

$$f(E,\mu) = \frac{1}{(1+e^{([E-\mu]/k_BT)})} \quad (80)$$

Here, V_{bias} is bias voltage, μ is the chemical potential of the electrodes. Γ_B, Γ_T correspond to the coupling strengths of the bottom and top electrodes, E_n corresponds to the orbital of the molecule, and T(E) is the sum over transmission coefficients of each orbital level of the molecule. T(E) can be expressed solely in terms of the HOMO level, since the charge transport occurs mainly at the closest frontier orbital level.

In addition, I introduced the asymmetric factor α into T(E). Conventionally in molecular electronics, asymmetry of a junction have been expressed only through coupling terms, Γ_B, Γ_T by assuming the position of molecular orbital (MO) level to be shifted about $(1/2 - \eta)\times V_{bias}$ with $\eta = \Gamma_B/(\Gamma_T + \Gamma_B)$.[92-94] However, since the interfacial coupling is not the only factor determining the asymmetry, the new asymmetric factor α, independent of Γ, was introduced to replace η. In motivation of phenomenologically describing the MO level shift, α was chosen to directly reveal the proportion of the voltage drop occurring at the MO level to the total bias by expressing MO level as $(E_{MO} - \alpha V_{bias})$. In this configuration, the asymmetry was realized as the tunneling barrier height ($E_0 = E_f - E_{HOMO}$) shifts $\alpha \times V_{bias}$ in the left side and $(1-\alpha)\times V_{bias}$ in the opposite side when V_{bias} is applied. In detail, when the bottom electrode is more strongly coupled, then α > 0.5, oppositely α < 0.5, and the case of α = 0.5 corresponds to the symmetric case. For instance, a series of experiments on Ferroceneyl-undecanethiol (FcC11) molecule have shown that Au-FcC11-EGaIn (Euthetic-GaIn) device structure, α for the HOMO of Fc moiety was about 0.7.[93-98]

Additionally, I gave some modifications to the coupling constant Γ_X (X= B or T). Coupling term Γ_X, which can also be interpreted as a broadening term (or escape rate to molecular channel from contacts), is generally given by [99]

$$\Gamma_X(E) = \sum_{Xn} \frac{|\tau_X|^2 0^+}{(E-E_{Xn})^2+(0)^+} \tag{81}$$

where $|\tau_X|$ refers molecule-electrode coupling strength term, E_{Xn} is an orbital level of the reservoir and 0^+ is an positive arbitrary infinitesimal. Since conductive electrodes such as Au or graphene consist of very closely spaced energy levels, I can replace the above summation into integral form, and by neglecting infinitesimal constant 0^+, this can be reduced into Equation 82,[99]

$$\Gamma_X(E) = \int d\varepsilon_X D_X(\varepsilon_X) \frac{|\tau_X|^2 0^+}{(E-E_X)^2+(0)^+} \approx 2\pi D_X(E)|\tau_X|^2 \tag{82}$$

Based on this, I replaced Γ_X by $\Gamma_{X0} \times D_X(E)$, where $D_X(E)$ is the electrodes' DOS and Γ_{X0} is the scaling factor, which is proportional to the coupling strength. For noble metals such as gold, I can regard the DOS $D_B(E) \sim \Theta(\mathrm{E})$ as a flat function. On the other hand, for the graphene electrode, if I suppose that electrons are transported into graphene almost horizontally, I can assume the DOS as

$$D_T(E) \sim (E-E_{dp})/\left(\hbar v_f\right)^2 \tag{83}$$

Additionally, the imperfection of our graphene was considered. The graphenes used in our experiments were inevidently exposed to PMMA, water, and various potential pollutant during the transfer process. Moreover, since our device used large CVD-grown graphene film as a few centimeters, it is definitely not a single crystal pristine graphene. Thereby the DOS of our

graphene would not ideally vanish at the Dirac point. To reflect such inhomogeneous broadening of our device, I replaced graphene's conical band structure into a hyperbolic one with a tiny dummy term D_{gr} to become ~$\sqrt{\left(E+E_{dp}+eV_{bias}\right)^2+D_{gr}}$. With all these assumptions, the final form of transmission coefficient used in our fitting is given by

$$T(E) \approx \frac{4\Gamma_{Lo} \times \Gamma_{Ro}\sqrt{\left(E+E_{dp}+eV_{bias}\right)^2+D_{gr}}}{\left(\left(\Gamma_{Lo}+\Gamma_{Ro}\sqrt{\left(E+E_{dp}+eV_{bias}\right)^2+D_{gr}}\right)^2+(E-E_{HOMO}+\alpha eV)^2\right)} \tag{84}$$

3.2. Analysis of Charge Transports in Molecular Junctions under Light Illumination

Substituting the corrections on transmission coefficients given in the previous sections, I can describe the resonant tunneling current via Equation (5)**,** which is used to fit the average I−V curves of BPT (Figure 15a) and PFBT molecular junctions (Figure 15b).[47, 66] where E is the energy of the charge carrier, $f_X(E)$ is the Fermi-Dirac distribution of each electrode given by Equation (4), and $T(E,V)$ is the transmission function given by Equation (80). where μ_X is the Fermi level of electrodes and X = top or bottom, and Γ_X is the electronic coupling strength between SAM and respective electrode X(B:Bottom, T:Top), E_0 is the energetic difference between the frontier orbital (HOMO level in this study) and the Fermi level of each electrode, and α is the asymmetric factor. Asymmetry factor α, which indicates how much the molecular orbital level is shifted when a bias is applied, takes a value of 0.5 for a symmetric junction. For example, the α value was assumed to be 0.7 for the Au/ferrocene/eutectic gallium-indium (EGaIn) structure, as in several previous studies.[17,18, 67-70]

In our case, respective asymmetric factors were determined through the fitting process since there have been no known values for our molecular junction structures. The detailed fitting

procedure is described in next section. Briefly speaking, local minimum values of E_0 and Γ_X were found by grid search, and converged values were obtained by gradient-descent methods. Extracted transport parameters are summarized in Table 3.

Table 3. *Charge injection barriers (E_0), coupling constants (Γ_X), and asymmetric factors (α) extracted from the averaged I–V fitting curves by employing the Landauer formula.*

		Γ_B (meV)	Γ_T (meV)	E_0 (eV)	α
BPT	Dark	44	23	0.56	0.43
	Light	44	34	0.52	0.445
BDT	Dark	49	21	0.52	0.44
	Light	49	30	0.49	0.48
PFBT	Dark	50	40	0.8	0.42
	Light	50	115	0.75	0.45

Generally, it was observed that E_0 (tunneling barrier) decreased and Γ_T (coupling between SAM and graphene) increased for all molecules under the light condition; Both cases improve the current enhancement of molecular junctions. Specifically, the E_0 value decreased from 0.50 under the dark condition to 0.48 eV under the light illumination for BPT, from 0.52 to 0.49 eV for BDT, and from 0.8 to 0.75 eV for PFBT. I inferred that such light-driven barrier (E_0) reduction occurred as photo-generated holes were transferred to graphene (see Figure 15b for the band alignment). This phenomenon results in further p-type doping of graphene, which reduces the difference between the HOMO and the Fermi level of graphene. The Γ_B values, which represent the coupling strength between SAM and Au, did not change with illumination since the Au–S covalent bonding is almost unaffected by light. Since BDT and BPT make van

der Waals contacts with graphene,[71] their Γ_T values are relatively small under the dark condition compared to those for PFBT junctions, which form F–C semi-ionic bonding with graphene (see Section 15).[72] Under the light illumination, Γ_T values increased from 23 to 34 meV for BPT, from 21 to 30 meV for BDT, and from 40 to 115 meV for PFBT. Naturally, Γ_T values were less than Γ_B (44–50 meV) except the light condition of PFBT, since covalent bonds are more robust than ionic or van der Waals interactions. Asymmetric factor α values also increased after the light illumination, but unlike E_0 or Γ_T, any tendency by molecules was not observed. However, considering that α values approach 0.5 (symmetric) under light conditions, it seems that the light-induced p-doping of graphene helps to reduce asymmetry in the aspect of the band structure, further reducing the gap between Γ_B and Γ_T.

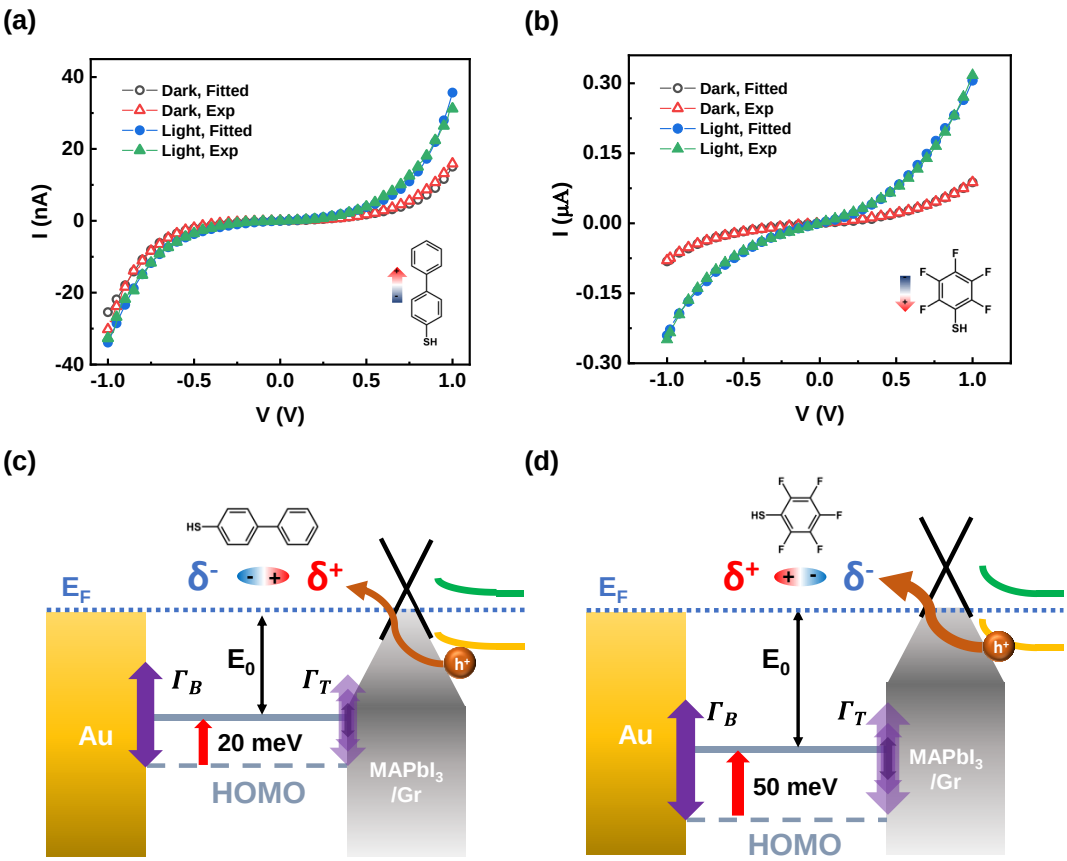

Figure 15. *(a, b) Fitting results of average I–V curves for (a) BPT and (b) PFBT molecular junctions by using Landauer formula. Black open circles: fitted I–V curves of the dark*

condition. Red open triangles: experimental data of the dark condition. Blue filled circles: fitted I–V data of the light condition. Green filled triangles: experimental curves of the light condition. (c, d) Schematic illustration of the charge transport modulation mechanism for (c) BTP and (d) PFBT molecular junctions.

Addtionally I also fitted the averaged I-V curves of the case of BDT molecular junctions. Figure 16 demonstrates the I–V curve fitting result of BDT-based molecular junctions. Experimental I–V curves are the average logarithmic current densities under dark and light conditions. Extracted Γ_B, Γ_T, E_0, and α are listed in Table 3.

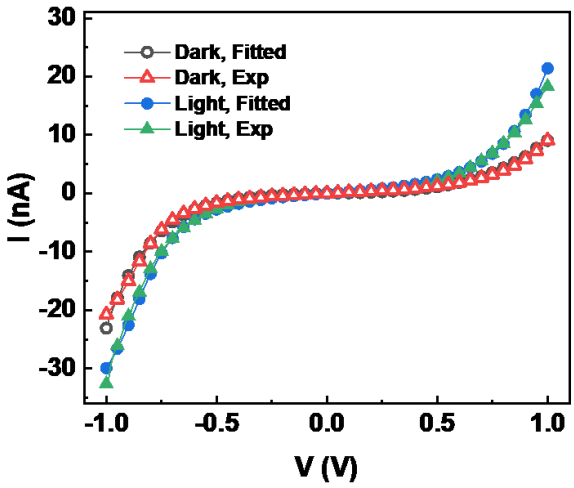

Figure 16. *I–V curve fitting of BDT-based molecular junctions.*

3.3. Detailed Fitting procedure of the Landauer formalism

To fit the I–V characteristics, I firstly computed the Equation. 78 with T(E) in the form of Equation. 84, and manually adjusted involved parameters to find their adequate range, where the fitting curve best resembles experimental I–V data. Integrals in this process were conducted only from E = –3 to E = +3 eV, the range in which the integrand almost converges, considering

that the HOMO-LUMO gaps of molecules can be accessed within the specified range of the applied bias voltage (see Table 2). Additionally, since such calculations are based on the current flow through a single molecule, computed current values should be multiplied by the total number of molecules in junctions for fitting. However, since the conductance per molecule is drastically reduced in a large-area molecular junction compared to that of a single molecule junction as empirically known,[100] I took this discrepancy factor by normalizing the computed current for each fitting process.

From Equation. 84, I chose E_{HOMO}, the coupling with the bottom electrode Γ_{B0} and the top electrode Γ_{T0}, and asymmetric factor α as candidates for our fitting parameters. In order to obtain accurate fits, I reduced the number of fitting parameters with several steps. From our inspection of the contribution of each fitting parameter, it was found that α varies the asymmetry of the curve, and E_0 (= $|E_f - E_{HOMO}|$) mainly determines the overall curvature and magnitude of the curve, while Γ contributes to all the aforementioned features. Among these parameters, the fitting behavior was the most sensitive to α, and therefore the fitting was only feasible within any appropriate range. I manually found these α ranges with many trials (consequently from 0.35 to 0.45). By changing the α values obtained in advance (with 0.005 steps), I searched the most suitable values of Γ_B, Γ_T, and E_0 for describing the I–V characteristics of the BPT device under the dark condition. During the process, I excluded physically unreasonable results, such as Γ_T being greater than Γ_B (i.e. the coupling between the Au-S covalent bonding at the bottom electrode is expected to be bigger). Under the light condition, Γ_B is assumed to remain constant since Au-S bonding is expected to be insensitive to light illumination, so only Γ_T and E_{HOMO} became major fitting parameters. By grid searching, I found a set of variables that minimizes root-mean-squared (RMS) differences between the experimental and the fitted I–V curves. A small dummy term (D_{gr}) was also fixed and tested only for a few cases for the same reason.

As a result, for the BPT and BDT junctions, I set the range of Γ_T from 20 to 40 meV and E_0 from 0.45 to 0.55 eV with each variable divided into 50 and 20 grids, respectively. I eventually computed the total of 1000 fitted I–V curves and compared the RMS differences between each set of computed and experimental curves to find the optimal set of Γ_T and E_0 that minimizes the RMS value. For the PFBT junctions, I changed the Γ_T range from 30 to 50 meV for dark and 100 to 120 for light, and E_0 from 0.65 to 0.85 eV, with the same number of grids. The final extracted parameters are listed in Table 3.

3.4. Evidence of C-F Semi-ionic bonds Formation between PFBT and Graphene

In additon, in order to support the claim that PFBT molecules form F-C semi-ionic bonding with graphene I conducted X-ray Photoelectron Spectroscopy (XPS) measurement. From the Au/PFBT/graphene heterostructure sample, I could identify the peaks that represent C-F bonds in C1s XPS (Figure 17(a)) and F1s XPS (Figure 17(b)), from which I determined the types of C-F bonds present in the molecular junctions. For the C1s XPS, ionic bond (~3.0 Å) peak, semi-ionic bond (~1.7 Å) peak, and covalent bond (~1,4 Å) peaks should be observed near ~285 eV, ~287.5 eV, and ~291 eV, respectively, whereas C=C bonds are observed at 284.4 eV.[101] From the data I obtained in Figure 17(a), I could identify the peak representing sp^2 bond at 284.5 eV (i.e. from graphene) and the C-F peak at 287 eV which I assign as semi-ionic bonds. This is consistent with the F1s XPS (Figure 17(b)), where the semi-ionic bonding nature of the C-F bond can be identified as a peak near 686 - 687 eV, while covalent bonds should appear near 690 eV.[102] From Figure 17(b), I can clearly observe the peak at 687.5 eV, thus supporting our prediction that C-F semi-ionic bond is formed between the F atom of the PFBT molecule and C of graphene.

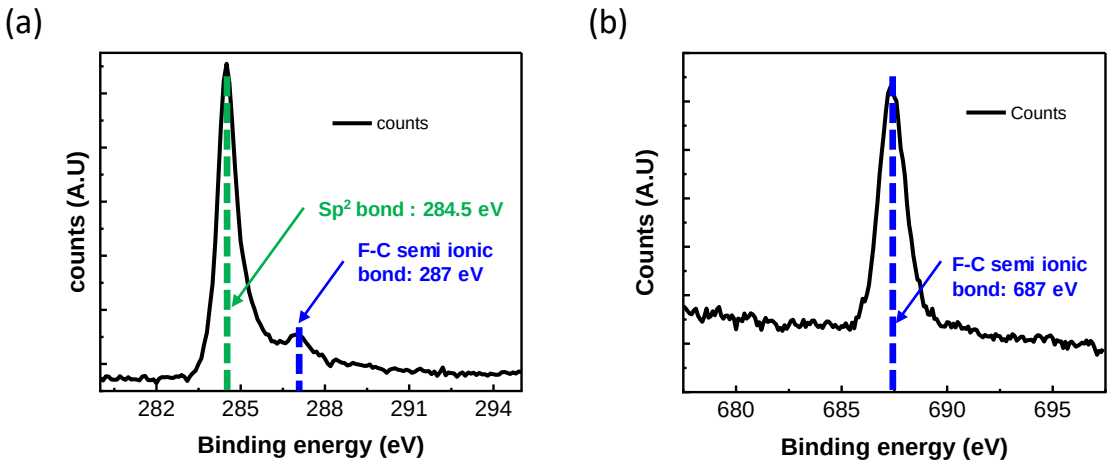

Figure 17. *From the Au/PFBT/graphene heterostructured sample, I extracted (a) peaks of C-F bonds in C1s XPS. (b) peaks of C-F bonds in F1s XPS.*

These barrier reduction and photoinduced coupling enhancement effects were the smallest in BPT and largest in PFBT, which is consistent with the observed photoinduced current enhancement as described above. The significant difference in their photoresponsivity can be accounted for by the dipole direction which is expected to modulate hole injection, and therefore inducing the E_0 shift. Furthermore, given that the Γ_T increase was higher for PFBT than for the other molecules, I can deduce that the dipole moment is also related to the observed photoinduced coupling enhancement. Unlike BPT or BDT, the δ^- partial charges of PFBT SAM attract numerous holes to graphene and strongly pull each other through Coulombic interaction, causing a considerable Γ_T increase and therby improving the charge transport. Consequently, as depicted in Figures 15c and 15d, the underlying mechanism of photoinduced charge transport in $MAPbI_3$/graphene/SAM/Au molecular junctions can be summarized to the enhanced hole injection via E_0 lowering and Γ_T enhancement at the interface between the SAM monolayer and the top graphene/$MAPbI_3$/electrode, both of which are assisted by the molecular dipole moments.

4. Summary

In summary, I implemented the concept of attaining photoresponsivity in molecular junctions with intrinsically low photoresponsivity by employing a photoactive electrode consisting of $MAPbI_3$/graphene heterostructure. The photogenerated holes in $MAPbI_3$ undergo internal-field-assisted charge transfer to graphene which triggered a significant photoinduced current enhancement in various molecular junctions. Our results clearly indicate a critical role of the SAM channel in enhancing the photocurrent generation. Firstly, an order of magnitude photoinduced current enhancement was demonstrated by adopting different transport regimes from non-resonant to resonant tunneling according to relative frontier orbital levels of different molecules. The photocurrent could be further enhanced (max. PDR of 1000%) by rationally selecting molecules with intrinsic dipole moments that can field-assist the charge transfer at the SAM/graphene interface. The theoretical analysis using the Landauer formalism revealed that the photoinduced energy barrier lowering and coupling effects are responsible for inducing the photocurrent in the molecular junctions. Our results demonstrate a heuristic design of photoresponsive molecular junctions via strategic construction of the molecular active channel and heterointerfaces, in addition to the analytical framework of the charge transport that can be expanded to various molecular-based hybrid optoelectronic devices.

References

[1] J. M. Beebe, B. Kim, J. W. Gadzuk, C. D. Frisbie, J. G. Kushmerick, Phys. Rev. Lett. **2006**, 97, 026801.

[2] H. Park, J. Park, A. K. L. Lim, E. H. Anderson, A. P. Alivisatos, P. L. McEuen, Nature **2000**, 407, 57.

[3] M. A. Reed, C. Zhou, C. J. Muller, T. P. Burgin, J. M. Tour, Science **1997**, 278, 252.

[4] W. Y. Wang, T. Lee, M. A. Reed, Phys. Rev. B **2003**, 68.

[5] B. Q. Xu, N. J. J. Tao, Science **2003**, 301, 1221.

[6] N. Xin, J. Guan, C. Zhou, X. Chen, C. Gu, Y. Li, M. A. Ratner, A. Nitzan, J. F. Stoddart, X. Guo, Nat. Rev. Phys. **2019**, 1, 211.

[7] C. Jia, A. Migliore, N. Xin, S. Huang, J. Wang, Q. Yang, S. Wang, H. Chen, D. Wang, B. Feng, Z. Liu, G. Zhang, D.-H. Qu, H. Tian, M. A. Ratner, H. Q. Xu, A. Nitzan, X. Guo, Science **2016**, 352, 1443.

[8] D. Xiang, X. Wang, C. Jia, T. Lee, X. Guo, Chem. Rev. **2016**, 116, 4318.

[9] H. Fu, X. Zhu, P. Li, M. Li, L. Yang, C. Jia, X. Guo, J. Mater. Chem. C, DOI: 10.1039/D1TC04079K.

[10] F. Schwarz, G. Kastlunger, F. Lissel, C. Egler-Lucas, S. N. Semenov, K. Venkatesan, H. Berke, R. Stadler, E. Lortscher, Nat. Nanotechnol. **2016**, 11, 170.

[11] L. J. Cui, R. J. Miao, K. Wang, D. Thompson, L. A. Zotti, J. C. Cuevas, E. Meyhofer, P. Reddy, Nat. Nanotechnol. **2018**, 13, 122.

[12] H. Song, Y. Kim, Y. H. Jang, H. Jeong, M. A. Reed, T. Lee, Nature **2009**, 462, 1039.

[13] M. Paulsson, S. Datta, Phys. Rev. B **2003**, 67, 241403.

[14] P. Reddy, S.-Y. Jang, R. A. Segalman, A. Majumdar, Science **2007**, 315 ,1568

[15] S. Park; H. J. Yoon, Nano Letters **2018**, 18, 7715.

[16] S. Park, J. Jang, H. Kim, D. I. Park, K. Kim, H. J. Yoon, Journal of Materials Chemistry A **2020**, 8, 19746.

[17] C. A. Nijhuis, W. F. Reus, G. M. Whitesides, J. Am. Chem. Soc. **2010**, 132, 18386.

[18] C. A. Nijhuis, W. F. Reus, J. R. Barber, M. D. Dickey, G. M. Whitesides, Nano Lett. **2010**, 10, 3611.

[19] V. B. Engelkes, J. M. Beebe, C. D. Frisbie, J. Am. Chem. Soc. **2004**, 126, 14287.

[20] B. Kim, S. H. Choi, X. Y. Zhu, C. D. Frisbie, J. Am. Chem. Soc. **2011**, 133, 19864.

[21] X. P. Chen, M. Roemer, L. Yuan, W. Du, D. Thompson, E. del Barco, C. A. Nijhuis, Nat. Nanotechnol. **2017**, 12, 797.

[22] G. D. Kong, J. Jin, M. Thuo, H. Song, J. F. Joung, S. Park, H. J. Yoon, J. Am. Chem. Soc. **2018**, 140, 12303.

[23] G. D. Kong, M. Kim, H.-J. Jang, K.-C. Liao, H. J. Yoon, Phys. Chem. Chem. Phys. **2015**, 17, 13804.

[24] J. C. Love, L. A. Estroff, J. K. Kriebel, R. G. Nuzzo, G. M. Whitesides, Chem. Rev. **2005**, 105, 1103.

[25] H. B. Akkerman, P. W. M. Blom, D. M. de Leeuw, B. de Boer, Nature **2006**, 441, 69.

[26] R. C. Chiechi, E. A. Weiss, M. D. Dickey, G. M. Whitesides, Angew. Chem. Int. Ed. **2008**, 47, 142.

[27] G. Wang, Y. Kim, S. I. Na, Y. H. Kahng, J. Ku, S. Park, Y. H. Jang, D. Y. Kim, T. Lee, J. Phys. Chem. C **2011**, 115, 17979.

[28] Y. Jang, S. J. Kwon, J. Shin, H. Jeong, W. T. Hwang, J. Kim, J. Koo, T. Y. Ko, S. Ryu, G. Wang, T. W. Lee, T. Lee, ACS Appl. Mater. Interfaces **2017**, 9, 42043.

[29] M. Min, S. Seo, S. M. Lee, H. Lee, Adv. Mater. **2013**, 25, 7045.

[30] D. Kos, D. R. Assumpcao, C. Y. Guo, J. J. Baumberg, ACS Nano **2021**, 15, 14535.

[31] A. M. Najarian, R. L. McCreery, ACS Nano **2019**, 13, 867.

[32] T. Sendler, K. Luka-Guth, M. Wieser, Lokamani, J. Wolf, M. Helm, S. Gemming, J. Kerbusch, E. Scheer, T. Huhn, A. Erbe, Adv. Sci. **2015**, 2, 1500017.

[33] D. Kim, H. Jeong, W. T. Hwang, Y. Jang, D. Sysoiev, E. Scheer, T. Huhn, M. Min, H. Lee, T. Lee, Adv. Funct. Mater. **2015**, 25, 5918.

[34] J. Koo, Y. Jang, L. Martin, D. Kim, H. Jeong, K. Kang, W. Lee, J. Kim, W. T. Hwang, D. Xiang, E. Scheer, M. Kabdulov, T. Huhn, F. Pauly, T. Lee, ACS Appl. Mater. Interfaces **2019**, 11, 11645.

[35] S. Seo, M. Min, S. M. Lee, H. Lee, Nat. Commun. **2013**, 4, 1920.

[36] M. A. Green, A. Ho-Baillie, H. J. Snaith, Nat. Photonics **2014**, 8, 506.

[37] B. R. Sutherland, E. H. Sargent, Nat. Photonics **2016**, 10, 295.

[38] H. J. Snaith, Nat. Mater. **2018**, 17, 372.

[39] J. Kim, W. Lee, K. Cho, H. Ahn, J. Lee, K.-Y. Baek, J.-K. Kim, K. Kang, T. Lee, Nanotechnology **2021**, 32, 185203.

[40] M. A. Haque, M. I. Nugraha, S. H. K. Paleti, D. Baran, J. Phys. Chem. C **2019**, 123, 14928.

[41] A. H. Castro Neto, F. Guinea, N. M. R. Peres, K. S. Novoselov, A. K. Geim, Rev. Mod. Phys. **2009**, 81, 109.

[42] S. J. Kim, J. Ryu, S. Son, J. M. Yoo, J. B. Park, D. Won, E. K. Lee, S. P. Cho, S. Bae, S. Cho, B. H. Hong, Chem. Mater. **2014**, 26, 2332.

[43] W. Lee, J. Lee, H. D. Lee, J. Kim, H. Ahn, Y. Kim, D. Yoo, J. Lee, T. W. Lee, K. Kang, T. Lee, Sci. Rep. **2020**, 10.

[44] J. Lee, W. Lee, J. Lee, K. Y. Baek, J. Shin, J. K. Kim, J. Kim, H. Ahn, K. Kang, T. Lee, Adv. Mater. Technol. **2021**, 6, 202001131.

[45] J. M. Tour, L. Jones, D. L. Pearson, J. J. S. Lamba, T. P. Burgin, G. M. Whitesides, D. L. Allara, A. N. Parikh, S. Atre, J. Am. Chem. Soc. **1995**, 117, 9529.

[46] Y. Kim, T. Pietsch, A. Erbe, W. Belzig, E. Scheer, Nano Lett. **2011**, 11, 3734.

[47] E. Scheer, J. C. Cuevas, Molecular Electronics: An Introduction to Theory and Experiment Wolrd Scientific Publishing Co., Singapore **2010**. 638

[48] Y. Lee, J. Kwon, E. Hwang, C.-H. Ra, W. J. Yoo, J.-H. Ahn, J. H. Park, J. H. Cho, Adv. Mater. **2015**, 27, 41.

[49] Y. Wang, Y. Zhang, Y. Lu, W. Xu, H. Mu, C. Chen, H. Qiao, J. Song, S. Li, B. Sun, Y.-B. Cheng, Q. Bao, Adv. Opt. Mater. **2015**, 3, 1389.

[50] P.-H. Chang, S.-Y. Liu, Y.-B. Lan, Y.-C. Tsai, X.-Q. You, C.-S. Li, K.-Y. Huang, A.-S. Chou, T.-C. Cheng, J.-K. Wang, C.-I. Wu, Sci. Rep. **2017**, 7, 46281.

[51] O. Malinkiewicz, A. Yella, Y. H. Lee, G. M. Espallargas, M. Graetzel, M. K. Nazeeruddin, H. J. Bolink, Nat. Photonics **2014**, 8, 128.

[52] M. Caputo, N. Cefarin, A. Radivo, N. Demitri, L. Gigli, J. R. Plaisier, M. Panighel, G. Di Santo, S. Moretti, A. Giglia, M. Polentarutti, F. De Angelis, E. Mosconi, P. Umari, M. Tormen, A. Goldoni, Sci. Rep. **2019**, 9, 15159.

[53] P. Schulz, E. Edri, S. Kirmayer, G. Hodes, D. Cahen, A. Kahn, Energy Environ. Sci. **2014**, 7, 1377.

[54] Z. Zhu, J. Ma, Z. Wang, C. Mu, Z. Fan, L. Du, Y. Bai, L. Fan, H. Yan, D. L. Phillips, S. Yang, J. Am. Chem. Soc. **2014**, 136, 3760.

[55] R. S. Yan, Q. Zhang, W. Li, I. Calizo, T. Shen, C. A. Richter, A. R. H. Walker, X. L. Liang, A. Seabaugh, D. Jena, H. G. Xing, D. J. Gundlach, N. V. Nguyen, Appl. Phys. Lett. **2012**, 101, 022105.

[56] R. M. Feenstra, D. Jena, G. Gu, J. Appl. Phys. **2012**, 111, 043711.

[57] Y. Yin, Z. G. Cheng, L. Wang, K. J. Jin, W. Z. Wang, Sci. Rep. **2014**, 4, 5758.

[58] S. S. Pingale, Physical Chemistry Chemical Physics **2011**, 13, 15158.

[59] H. J. Yoon, N. D. Shapiro, K. M. Park, M. M. Thuo, S. Soh, G. M. Whitesides, Angewandte Chemie International Edition **2012**, 51, 4658.

[60] H. J. Yoon, C. M. Bowers, Mo. Baghbanzadeh, G. M. Whitesides, Journal of the American Chemical Society **2014**, 136, 16.

[61] M. Baghbanzadeh, L. Belding, L. Yuan, J. Park, M. H. Al-Sayah, C. M. Bowers, G. M. Whitesides, Journal of the American Chemical Society **2019**, 141, 8969.

[62] J. S. Eo, J. Shin, S. Yang, T. Jeon, J. Lee, S. Choi, C.-H. Lee, G. Wang, Advanced Science **2021**, 8, 2101390.

[63] H. Kang, S. Seong, E. Ito, T.Isoshima, M. Hara, H. J. Yoon, J. Noh, Applied Surface Science **2021**, 555, 149671.

[64] J. G. Simmons, J. Appl. Phys. **1963**, 34, 1793.

[65] X. Guo, Molecular-Scale Electronics: Current Status and Perspectives, Springer, Cham, Switzerland **2018**. 377

[66] S. Datta, Quantum Transport : Atom to Transistor, Cambridge University Press, New York, USA **2005**. 404

[67] G. Wang, Y. Kim, S.-I. Na, Y. H. Kahng, J. Ku, S. Park, Y. H. Jang, D.-Y. Kim, T. Lee, J. Phys. Chem. C **2011**, 115, 17979.

[68] Y. Jang, S.-J. Kwon, J. Shin, H. Jeong, W.-T. Hwang, J. Kim, J. Koo, T. Y. Ko, S. Ryu, G. Wang, T.-W. Lee, T. Lee, ACS Appl. Mater. Interfaces **2017**, 9, 42043.

[69] N. Nerngchamnong, L. Yuan, D.-C. Qi, J. Li, D. Thompson, C. A. Nijhuis, Nat. Nanotechnol. **2013**, 8, 113.

[70] C. A. Nijhuis, W. F. Reus, G. M. Whitesides, J. Am. Chem. Soc. **2009**, 131, 17814.

[71] Y. Jang, H. Jeong, D. Kim, W.-T. Hwang, I. Jeong, H. Song, H. Jeong, M. Min, T. Lee, J. Nanosci. Nanotechnol. **2016**, 16, 8565.

[72] J. Kim, R. Zhou, K. Murakoshi, S. Yasuda, RSC Adv. **2018**, 8, 14152.

[73] M. I. Saidaminov, A. L. Abdelhady, B. Murali, E. Alarousu, V. M. Burlakov, W. Peng, I. Dursun, L. Wang, Y. He, G. Maculan, A. Goriely, T. Wu, O. F. Mohammed, O. M. Bakr, Nat. Commun. **2015**, 6, 7586.

[74] L. Yuan, L. Jiang, D. Thompson, C. A. Nijhuis, J. Am. Chem. Soc. **2014**, 136, 6554.

[75] S. K. Karuppannan, H. Hongting, C. Troadec, A. Vilan, C. A. Nijhuis, Adv. Funct. Mater. **2019**, 29, 1904452.

[76] A. Arakcheeva, D. Chernyshov, M. Spina, L. Forro, E. Horvath, Acta Cryst. **2016**, B72, 716.

[77] P.-H. Chang, S.-Y. Liu, Y.-B. Lan, Y.-C. Tsai, X.-Q. You, C.-S. Li, K.-Y. Huang, A.-S. Chou, T.-C. Cheng, J.-K. Wang, C.-I. Wu, Sci. Rep. **2017**, 7, 46281.

[78] S. M. Sze, K. K. Ng, Physics of Semiconductor Devices John Wiley & Sons, New Jersey, USA **2007**.

[79] R. S. Yan, Q. Zhang, W. Li, I. Calizo, T. Shen, C. A. Richter, A. R. H. Walker, X. L. Liang, A. Seabaugh, D. Jena, H. G. Xing, D. J. Gundlach, N. V. Nguyen, Appl. Phys. Lett. **2012**, 101, 022105.

[80] R. M. Feenstra, D. Jena, G. Gu, J. Appl. Phys. **2012**, 111, 043711.

[81] D. Kim, H. Jeong, W. T. Hwang, Y. Jang, D. Sysoiev, E. Scheer, T. Huhn, M. Min, H. Lee, T. Lee, Adv. Funct. Mater. **2015**, 25, 5918.

[82] J. Koo, Y. Jang, L. Martin, D. Kim, H. Jeong, K. Kang, W. Lee, J. Kim, W. T. Hwang, D. Xiang, E. Scheer, M. Kabdulov, T. Huhn, F. Pauly, T. Lee, ACS Appl. Mater. Interfaces **2019**, 11, 11645.

[83] S. Seo, M. Min, S. M. Lee, H. Lee, Nat. Commun. **2013**, 4, 1920.

[84] F. Neese, WIREs Comput. Mol. Sci. **2012**, 2, 73.

[85] F. Weigend, R. Ahlrichs, Phys. Chem. Chem. Phys. **2005**, 7, 3297.

[86] F. Weigend, Phys. Chem. Chem. Phys. **2006**, 8, 1057.

[87] F. Neese, F. Wennmohs, A. Hansen, U. Becker, Chem. Phys. **2009**, 356, 98.

[88] A. Petritz, M. Krammer, E. Sauter, M. Gärtner, G. Nascimbeni, B. Schrode, A. Fian, H. Gold, A. Cojocaru, E. Karner-Petritz, R. Resel, A. Terfort, E. Zojer, M. Zharnikov, K. Zojer, B. Stadlober, Adv. Funct. Mater. **2018**, 28, 1804462.

[89] Y. Kuzumoto, M. Kitamura, Appl. Phys. Express **2014**, 7, 035701.

[90] J. G. Simmons, J. Appl. Phys. **1963**, 34, 1793.

[91] E. H. Huisman, C. M. Guédon, B. J. van Wees, S. J. van der Molen, Nano Lett. **2009**, 9, 3909.

[92] K. Moth-Poulsen, Handbook of Single-Molecule Electronics, Pan Stanford Publishing, Singapore, 2016

[93] G. Wang, Y. Kim, S.-I. Na, Y. H. Kahng, J. Ku, S. Park, Y. H. Jang, D.-Y. Kim, T. Lee, J. Phys. Chem. C **2011**, 115, 17979.

[94] Y. Jang, S.-J. Kwon, J. Shin, H. Jeong, W.-T. Hwang, J. Kim, J. Koo, T. Y. Ko, S. Ryu, G. Wang, T.-W. Lee, T. Lee, ACS Appl. Mater. Interfaces **2017**, 9, 42043.

[95] C. A. Nijhuis, W. F. Reus, G. M. Whitesides, J. Am. Chem. Soc. **2010**, 132, 18386.

[96] C. A. Nijhuis, W. F. Reus, J. R. Barber, M. D. Dickey, G. M. Whitesides, Nano Lett. **2010**, 10, 3611.

[97] N. Nerngchamnong, L. Yuan, D.-C. Qi, J. Li, D. Thompson, C. A. Nijhuis, Nat. Nanotechnol. **2013**, 8, 113.

[98] C. A. Nijhuis, W. F. Reus, G. M. Whitesides, J. Am. Chem. Soc. **2009**, 131, 17814.

[99] S. Datta, Quantum Transport : Atom to Transistor, Cambridge University Press, New York, USA **2005**.404

[100] H. B. Akkerman, B. de Boer, J. Phys. Condens. Matter **2007**, 20, 013001.

[101] W.Feng, P.Long, Y.Feng, Y.Li, Adv.Sci.**2016**, 3, 1500413

[102] P. V.Bakharev, M.Huang, M.Saxena, S.W.Lee, S.H.Joo, S.O.Park,; J.Dong, D.C. Camacho-Mojica, S.Jin, Y.Kwon, M.Biswal, F.Ding, S.K.Kwak, Z.Lee, R.S Ruoff, Nat. Nanotech. **2020**, 15, 59.

국 문 초 록

감광성은 광전기능의 핵심요소로 이를 분자소자에서 구현하고자 하는 시도가 오랫동안 이루어져 왔습니다. 이를 위해 분자 접합 소자에서 가장 많이 채택되는 전략 중 하나는 전도 채널에 광활성 분자를 사용하는 것 입니다. 그러나 이러한 소자는 상대적으로 낮은 감광도, 긴 스위칭 시간 및 빛에 의한 비가역적 변화라는 문제가 있습니다. 이 연구에서는 SAM(self-assembled monolayer: 자기조립단분자막) 기반 분자 접합에서, 광활성 유기 할로겐화물 페로브스카이트(organo-halide perovskite, OHP)/ 그래핀 이종접합을 전극으로 채용하여 기존과는 다른 가역적 광전 소자를 구현하였습니다. 페로브스카이트/ 그래핀/ SAM 의 하이브리드 소자 구조는 분자 접합부가 본질적으로 광 반응이 거의 없는 분자임에도 다소 높은 광 반응성을 얻을 수 있게 합니다. 더 나아가 서로 다른 고유 쌍극자 모멘트를 가진 분자를 사용한 소자에서 그래핀/SAM 계면의 전자구조가 형성되는 양상을 이론과 실험 모두를 분석함으로써, 분자 SAM 의 특성이 어떻게 광전류 특성을 제어하는지 그 원리를 파악하고, 이를 바탕으로 광감응성을 극대화시키는 소자를 구현하였습니다. 분자 오비탈 매개 공진 터널링 수송 체계 내에서 이루어진 계산과 분석은 이 연구에서의 소자의 밴드구조가 어떤 식으로 형성되는지에 대한 그림을 제시하였습니다. 이러한 이종접합 인터페이스가 있는 분자소자에서 광 유도 전하 수송에 대한 전반적 이해 향상은 향후 하이브리드 소자 아키텍처를 기반으로 하는 고성능 분자 광전자 장치를 설계하기 위한 이정표를 제시할 것으로 기대됩니다.

주요어: 분자전자학, 광전현상, 유기할라이드 페로브스카이트, 자기-조립단분자막, 그래핀 전극, 공명 터널링

학 번: 2020-21713